

LIGO 3 Strawman Design, Team Red

B. Barr¹, A. Bell¹, C. Bell¹, C. Bond², D. Brown², F. Brueckner², L. Carbone², K. Craig¹,
A. Cumming¹, S. Danilishin³, K. Dooley⁴, A. Freise², T. Fricke⁴, P. Fulda², S. Giampsis⁵,
N. Gordon¹, H. Grote⁴, G. Hammond¹, J. Harms⁶, S. Hild^{1,*}, J. Hough¹, S. Huttner¹, R. Kumar¹,
H. Lück⁴, N. Lockerbie⁷, J. Macarthur¹, I. Martin¹, P. Murray², S. Reid¹, S. Rowan¹,
D. Shoemaker⁸, B. Sorazu¹, K. Strain¹, S. Tarabrin⁴, K. Tokmakov¹ and N. Voronchev³

LIGO-T1200046-v1

Date: January 31, 2012

¹ SUPA, School of Physics and Astronomy, The University of Glasgow, Glasgow, G12 8QQ, UK

² University of Birmingham, Birmingham, B15 2TT, UK

³ Moscow State University, Moscow, 119992, Russia

⁴ Max-Planck-Institut für Gravitationsphysik and Leibniz Universität Hannover, D-30167 Hannover, Germany

⁵ University of Wisconsin-Milwaukee, Milwaukee, Wisconsin 53201, USA

⁶ California Institute of Technology, Pasadena, California 91125, USA

⁷ University of Strathclyde, Glasgow, G1 1XQ, UK

⁸ Massachusetts Institute of Technology, Cambridge, Massachusetts 02139, USA

*E-Mail: stefan.hild[at]glasgow.ac.uk



Contents

1	Executive Summary	3
2	Introduction	4
2.1	Beyond Advanced LIGO	4
2.2	Official Task Description for the Strawman Process	4
2.3	Strawman Red approach	4
3	Sensitivity	6
3.1	Sensitivity Calculations	6
3.2	Description of the Strawman Red Sensitivity	6
4	Suspension Thermal noise	9
4.1	Introduction	9
4.2	Suspension Upgrades	9
4.3	Performance benefit of the upgrades	12
4.4	Research plan towards reducing suspension thermal noise in LIGO-3	12
5	Newtonian Noise	14
5.1	Introduction	14
5.2	Current best estimates of Newtonian noise	14
5.3	NN mitigation techniques	15
5.3.1	Seismic shielding	15
5.3.2	Coherent noise subtraction using seismometer array data	16
5.4	Research plan towards reducing Newtonian noise in LIGO-3	17
5.4.1	Simulations of Newtonian noise and its cancellation at the LIGO sites	17
5.4.2	Experimental investigation of accelerometer array based noise cancellation	17
6	Coating Brownian	18
6.1	Overview	18
6.2	Increasing the beam size	18
6.3	Khalili cavities	19
6.4	Required Hardware for Khalili cavities	21
6.5	Optical coatings with reduced thermal noise	21
6.5.1	Continued improvement of tantala coatings	22
6.5.2	High-temperature annealing of coatings	23
6.5.3	Amorphous silicon as a high-index coating material	23
6.5.4	Crystalline coatings	23
6.6	Waveguide mirrors	24
6.7	Alternative Beam Shapes	27
7	Quantum noise	27
7.1	Introduction	27
7.2	Squeezing generation, injection, and detection losses	28
7.2.1	Squeezing generation	28
7.2.2	Optical isolation and injection	29
7.2.3	Mode matching	29
7.2.4	OMC loss and quantum efficiency of detection photodiodes	29
7.2.5	Losses due to phase noise and alignment signal split-off beams	29
7.2.6	Summary of squeezing losses	30
7.3	Filter cavity for frequency-dependent squeezing	30
7.4	Required Hardware	33
7.5	Alternative Solutions	33
7.5.1	Speedmeter	33
7.5.2	Local Readout schemes	33
8	Acknowledgements	36
A	Sagnac-Speedmeter with frequency dependent squeezing	36
	Bibliography	43



1 Executive Summary

In this document we describe a potential way to upgrade the Advanced LIGO interferometers beyond their baseline sensitivity. The aim of our considerations is to evaluate the potential sensitivity achievement for certain hardware changes, to identify key technologies required for such an upgrade, and to define the required R+D to be carried out over the next 5 years. The work presented here should be seen as first step on a very long way towards the realisation of these Advanced LIGO upgrades.

Upgrading of Advanced LIGO can in principle include any scale from minor changes of a secondary subsystem on the low effort end to a major rebuild of LIGO infrastructure or main interferometers at the high effort end. In order to narrow down the scope of our design investigations, we have chosen the following, somewhat arbitrary constraints:

- The upgrades should be available around 2018-2020.
- The cost of the upgrades of all Advanced LIGO interferometers would be limited to a total of 50-100 million USD.
- As the science case for Advanced LIGO upgrades is not well defined yet, we aim for a broadband sensitivity.

Based on these starting assumptions we developed a strawman design, which can provide a sensitivity improved at all frequencies above 8 Hz by a factor 3–4 compared to the Advanced LIGO baseline sensitivity (see lower subplot of Figure 2). This sensitivity corresponds to a binary neutron star (BNS) inspiral range of 614 Mpc (GWINC reported value) and an expected increase of the observed BNS inspiral event rate by roughly a factor of 30–40 in respect to the Advanced LIGO baseline (assuming a homogeneous distribution in space).

The main interferometer configuration of our design is quite similar to the Advanced LIGO baseline, i.e., a room temperature dual-recycled Michelson interferometer with arm cavities of 4 km and a circulating light power of about 800 kW. In order to reduce quantum noise we consider frequency dependent squeezing generated by reflection on a input filter cavity and an increase of the test mass weight to 160 kg. Coating Brownian noise will be reduced in two steps: First we will increase the beam size by a factor 1.6 and secondly we assume a further reduction by a factor 2 obtained from either the application of coatings with improved mechanical loss, or by replacing the dielectric coatings of the main test masses by resonant waveguide coatings, or by introducing anti-resonant end mirror cavities (so-called Khalili cavities). Sensitivity improvements at the low-frequency end of the observation band are achieved by increasing the length of the last pendulum stage to 1.2 m and by using seismometer signals for the subtraction of gravity gradient noise. A summary of the key design parameters can be found in Table 1.

A focus of our effort is the identification of R+D tasks required in order realise the described Advanced LIGO upgrade. Detailed R+D plans for the individual key technologies can be found in the corresponding noise chapters of this document.

Please note that the here described design represent just one potential example of what an Advanced LIGO upgrade might look like. It will take take years of intense R+D efforts until it will be possible to converge on an actual design. For the time being our design (in the following referred to as *Strawman Red*) might be helpful as reference for other design concepts and options to be compared against.



2 Introduction

2.1 Beyond Advanced LIGO

Currently the Advanced LIGO instruments are being installed and commissioned and are expected to reach their design sensitivity during the second third of this decade. Predicted rates for the observation of inspiraling binary neutron stars [1] suggest a high probability for the first direct detection of an astrophysical signal to take place in the second half of this decade. At that point in time (perhaps around 2018-2020) it might be possible to obtain a significant amount of funding for further sensitivity upgrades of Advanced LIGO. In order to be prepared for that time and have dummy blueprints of such upgrades ready in the drawer, now the required key-technologies, essential for these upgrades, have to be identified and a R&D-roadmap has to be developed to guide the research efforts over the next 5 years correspondingly. The work presented in this document aims to contribute to this exciting process.

At the beginning of November 2011 three design teams have been assembled and given 2 months of time for the development of so-called ‘*strawman designs*’. All three designs will then be presented at the beginning of January 2012 during a workshop at Caltech. This document serves as the documentation of the strawman design compiled by team red (in the following often referred to as ‘Strawman Red’).

2.2 Official Task Description for the Strawman Process

Email from Eric Gustafson to LSC-all from 25th Oct 2011: *During the last day of the LVC meeting in Gainsville there was a discussion session chaired by Rana Adhikari (chair of the Advanced Interferometer Configurations group) in which it was proposed that three teams be created to work through the details of three different “straw man” configurations for possible 3rd generation detectors. This design work would be followed by a competition comparing the different approaches. This is not a “real” competition for funding but instead an exercise to focus our thinking about what research and development we will need to do over the next few years to be in a position to build the next detector.*

2.3 Strawman Red approach

We assembled the Strawman Red team consisting of about 35 LSC-members from 8 different research institutions. Over the past two months the team was meeting regularly in telecons and about 25 team members participated in a 3-day workshop at the Glasgow observatory. Figure 1 gives a rough idea of how team red approached the strawman design.

In addition to the official strawman task description given in the previous section a set of assumptions and constraints was used as framework:

- The cost of the Advanced LIGO upgrade program was assumed to be limited to a maximum range of 50 to 100 million USD for all interferometers together.
- From the previous point one can deduce, that the considered upgrades have to use to a large extend the same vacuum infrastructure as Advanced LIGO. Therefore we assumed that moderate changes of the vacuum system in the central and end stations will be possible, but assumed that no changes to the 4 km long vacuum tubes are possible.
- In addition we assumed that the seismic pre-isolation system is off limits, as replacing it would probably not fit within the targeted budget.
- Regarding the anticipated timeline we assumed that all technologies included in our design should be mature enough to be compatible with an installation in 2018, assuming we start now with the required R&D and carry out the required prototyping over the next 5 years.

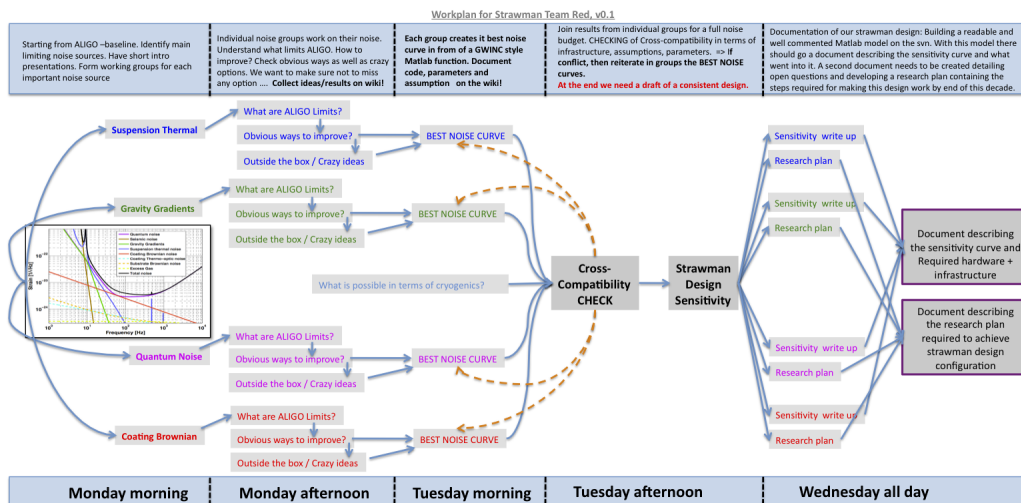


Figure 1: Original workplan of the Strawman Red team during a 3-day workshop in November 2011.

- Another assumption we made was to keep the test masses and their suspensions at room temperature.
- Due to the current lack of practical experience with compensation of thermal lensing effects in the few hundred kilowatt range, we also assumed that the Advanced LIGO upgrades will initially not use any higher circulating light power as in the Advanced LIGO baseline.
- Due to the limited time frame available for the strawman exercise we focussed our efforts nearly entirely on evaluating the ‘fundamental’ noise sources and in most cases did not consider implications on technical noise sources, such as control noise etc.
- Since at the current stage our focus was sent on identifying useful technologies for advanced LIGO upgrades, so far we did not perform any detailed parameter optimisation (on the percent level), to ‘squeeze’ the last few MPC of binary neutron star inspiral range out of Strawman Red.

Please note that all these assumptions mentioned above should just be seen as a working hypothesis for the Strawman Red design. Other teams will have chosen different working assumptions and may have included techniques in their design which we may have disregarded. This shows that at the current stage of the design process it is too early to exclude certain technologies and we should rather aim to find design options including a variety of different technologies and push the corresponding R&D efforts. Which technology will be used in the end for the Advanced LIGO upgrades will then become clearer and clearer over the next five years. Especially the experience gained during the commissioning of Advanced LIGO will help to identify the technologies providing the most robust and realistic design.

This openness in the Strawman designs is also reflected in this document: For instance we assume for the improvement of coating noise a reduction factor of 3.2. This factor 3.2 is the product of a factor 1.6 obtained by increasing the beam size correspondingly and another factor 2 which can come either from new coatings with improved mechanical properties, or the application of Khalili cavities, or the use of waveguide coatings. All three of these options are discussed in detail our document and only further experimental evaluations and progress in the prototyping over the next few years will show which of these three options will be the ‘optimal’ solution for the Advanced LIGO upgrade.

So please, see the rest of this document as an subjective example of what the Advanced LIGO upgrades **MAY** look like and not what they **WILL** or **WILL NOT** look like! The key task at the current stage of the progress is to identify and push forward the R&D required for allowing the advanced LIGO upgrades to be ready by the end of this decade.



3 Sensitivity

3.1 Sensitivity Calculations

Most of the noise and sensitivity curves presented in this document are based on GWINC¹. We used the Advanced LIGO GWINC code and parameter set as a starting point and then ‘modified’ the noise calculations in order to arrive at the Strawman Red noise budget. These modifications varied a lot for the different noise sources. For some noise sources (e.g., coating noise) we just modified the input parameters and/or introduced additional reduction factors, while for other noise sources we used functions of the GWINC development version² (e.g., quantum noise) or wrote our own calculations (e.g., suspension thermal noise).

3.2 Description of the Strawman Red Sensitivity

The full Strawman Red noise budget and the corresponding sensitivity described in this document is shown in Figure 2. The key parameters used for the calculation of this sensitivity are shown in Table 1. In the following list we give a brief overview of the assumed changes, while a more detailed description for each fundamental noise source can be found in the later sections of this document:

- **Suspension Thermal Noise:** We assumed fused silica suspensions at room temperature, with the length of the last stage being increased from 0.6 to 1.2 m. In addition the weight of the test mass was increased to 160 kg and the fibre geometry was accordingly adapted. These changes provide a suspension thermal noise reduction of about a factor 3 to 4 above 10 Hz.
- **Seismic Noise:** The increased length of the last suspension stage also improves the seismic noise by a factor 2. No subtraction techniques have been included.
- **Newtonian Noise:** We based our calculations on measured seismic data from LLO ETMX. We assumed a seismic level corresponding to the 90th percentile and an subtraction factor of 5. This turns out to be roughly equivalent to the 10th percentile without any subtraction.
- **Coating Thermal Noise:** We assumed an overall reduction of coating noise by a factor 3.2. Increasing the beam size by a factor 1.6 reduces the coating noise by a factor 1.6. In addition we assumed a further reduction of a factor 2 which can come from improved coatings or the application of Kahlili cavities or the use of waveguide mirrors or the application of alternative beam shapes.
- **Gas Noise:** Increasing the beam size on the test masses slightly reduces the gas noise.
- **Quantum noise:** We assumed the same interferometer configuration and optical power as for aLIGO. The quantum noise improvements originate from an increased test mass weight of 160 kg and the injection of frequency dependent squeezed light. We consider an initial squeezing level of 20 dB and losses of 9% plus the roundtrip loss in the filter cavity. The filtercavity has a length of 300 m and a roundtrip loss of 30 ppm.

The resulting sensitivity improvement in respect to the Advanced LIGO baseline is shown in the lower subplot of Figure 2. For all frequencies above 50 Hz the Strawman Red sensitivity can provide an improvement of a factor 3. In the range from 8 to 30 Hz the improvement is about a factor 4. The here presented sensitivity corresponds to an binary neutron star inspiral range of 614 MPc.

¹<https://awiki.ligo-wa.caltech.edu/aLIGO/GWINC>

²https://nodus.ligo.caltech.edu:30889/wiki/lib/exe/fetch.php?media=gwincdev_111109.tar.gz



Strawman Red Design Overview		
Subsystem and Parameters	Advanced LIGO Baseline Design	Strawman Red Design
Sensitivity		
Binary Neutron Star Inspiral Range	200 Mpc	614 Mpc
Anticipated Strain Sensitivity	$3.5 \cdot 10^{-24} / \sqrt{\text{Hz}}$ @ 300 Hz	$1.2 \cdot 10^{-24} / \sqrt{\text{Hz}}$ @ 250 Hz
Instrument Topology		
Interferometer	Dual-recycled Michelson with Armcavities	Dual-recycled Michelson with Armcavities
Quantum Noise Reduction	n.a.	Frequency-dependent input squeezing
Laser and Optical Parameters		
Laser Wavelength	1064 nm	1064 nm
Optical Power at Test Masses	730 kW	730 kW
Arm Cavity Finesse	450	450
Signal Recycling	$T = 20\%$, tuned	$T = 20\%$, tuned
Squeezing Factor	n.a.	20 dB
Filtercavity (FC) length	n.a.	300 m
FC Detuning	n.a.	-16.8 Hz
FC Input Mirror Transmittance	n.a.	425 ppm
Squeezing Losses	n.a.	9% + 30 ppm roundtrip in FC
Test Masses and Suspensions		
Mirror Material	Fused Silica	Fused Silica
Main Test Mass Diameter	35 cm	55 cm
Main Test Mass Weight	42 kg	160 kg
Masses in Main Quad (from top)	22 kg/22 kg/40 kg/40 kg	44 kg/66 kg/120 kg/160 kg
Masses in Reaction Chain (from top)	22 kg/22 kg/40 kg/40 kg	22 kg/22 kg/40 kg/40 kg
Total Mass of a Main Suspension	250 kg	520 kg
Length of Final Suspension Stage	0.6 m	1.2 m
Fused Silica Fibre Diameter	400 μm	566 μm
Fibre Diameter at Bending Point	800 μm	1624 μm
Coating Noise Reduction		
Improvement Factors	n.a.	factor 1.6 from increased beam size PLUS factor 2 from either (i) better coatings, OR (ii) Khalili cavities, OR (iii) waveguides
Operation Temperature	290 K	290 K
IM/EM ROC	1934/2245 m	1849/2173 m
IM/EM spotsize	5.31/6.21 cm	8.46/9.95 cm
Khalili cavity length	n.a.	50 m
Gravity Gradient Noise		
Assumed Seismic Level	???	LLO ETMX, 90th percentile
Assumed subtraction factor	n.a.	5

Table 1: Key design parameters of the Strawman Red configuration used to produce the sensitivity curve shown in Figure 2.

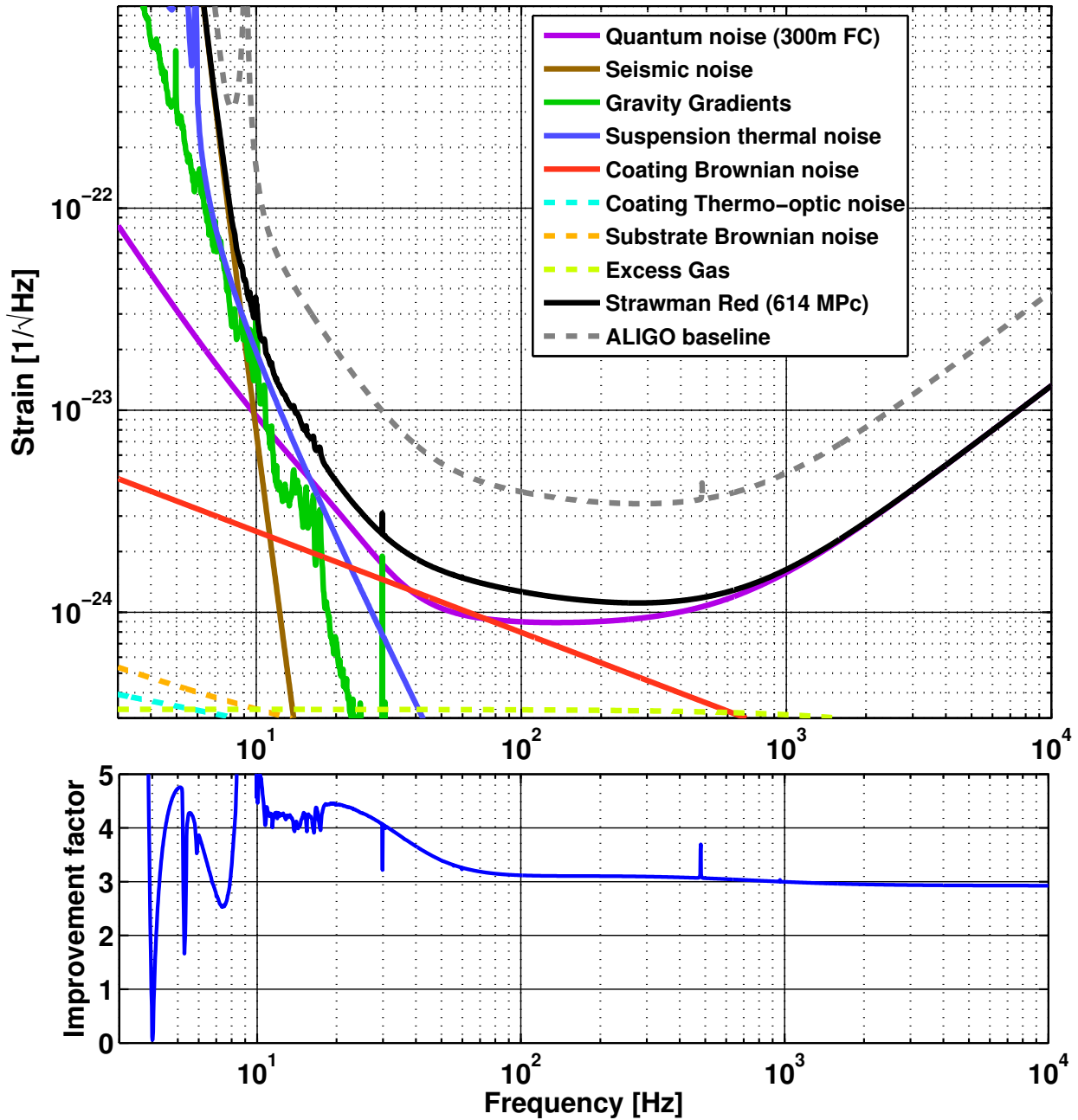


Figure 2: Noise budget for the LIGO-3 Strawman Red design (upper subplot) and the linear improvement factor compared to Advanced LIGO (lower subplot). The key parameters used to calculate this sensitivity curve can be found in Table 1.



4 Suspension Thermal noise

4.1 Introduction

At low frequencies (< 20 Hz) suspension thermal noise and seismic noise are important contributions to the total noise performance of the detector. It is instructive to briefly describe the aLIGO baseline before motivating methods to lower the suspension thermal noise in future upgrades (LIGO-3). The aLIGO baseline comprises four pendulum stages (the QUAD) with three stages of vertical isolation [2]. The vertical isolation performance is less demanding as any cross-coupling of vertical motion to horizontal motion is typically 0.1%. The final pendulum stage comprises the penultimate mass and test mass which are both 40 kg cylinders (diameter 34 cm and length 20 cm) of fused silica. Fused silica standoff ears are bonded to the side of the masses utilising hydroxide catalysis bonding [3]. Four fused silica fibres, which are pulled with a CO₂ laser, are welded onto the ears forming a quasi-monolithic final stage to lower suspension thermal noise [4, 5]. This method of attachment provides an ultra-low mechanical loss suspension by eliminating the need to utilise higher loss metal wires and eliminating friction that can occur at the metal wire clamping and break off points on the test mass.

Brownian thermal noise in the lower stage is conveniently calculated from the fluctuation-dissipation theorem and originates from mechanical dissipation in the ear/mass bond region [6], weld loss [7] at the fibre/ear attachment point, and bulk/surface/thermoelastic loss [8–10] in the fused silica fibres. The upper metal stages, although filtered by the final stage, add to the thermal noise through mechanical loss in the metal support wires and Maraging steel cantilever springs. The aLIGO fibre design is carefully optimised such that at the bending point the geometry of the fibre (or static stress) is chosen to null the thermoelastic noise contribution which would otherwise dominate. Techniques to characterize the thermal noise of the full suspension determine the bending energy stored in each portion of the suspension with the ANSYS Finite Element software [11]. The individual loss terms noted above can be evaluated at each point of the weld and fibre by scaling with the appropriate bending energy stored at that point in the suspension (i.e. a lossy region with zero stored bending energy will not contribute to the total loss angle). These loss terms are summed over the fibre to give the total mechanical loss, ϕ_t . A suspension fibre stores energy both in the elasticity of the material and the gravitational field. The latter term is lossless and dominates in heavily loaded suspension fibres. The dissipation dilution, or ratio of the total energy to the elastic energy, is conveniently calculated in Finite Element software and acts to reduce the total mechanical loss. The horizontal thermal displacement noise, above the pendulum resonance, is finally given by

$$x_{th}^2(\omega) = \frac{1}{D} \frac{k_B T}{2\pi^3 m f} \left(\frac{f_h^2 \phi_t(f)}{f_h^4 \phi_t^2(f) + (f_h^2 - f^2)^2} \right) \quad (1)$$

where D is the dissipation dilution, T is the temperature, m is the pendulum mass, $\phi(\omega)$ is the mechanical loss angle of the pendulum, f_h is the resonant frequency, k_B is Boltzmann's constant and f is the frequency. Vertical thermal noise also couples into the horizontal direction via the 0.1 % vertical-horizontal cross-coupling. The contribution to the horizontal thermal noise is thus given by

$$x_{th}^2(\omega) = \frac{1}{10^3} \frac{k_B T}{2\pi^3 m f} \left(\frac{f_v^2 \phi_t(f)}{f_v^4 \phi_t^2(f) + (f_v^2 - f^2)^2} \right) \quad (2)$$

where the dissipation dilution in the vertical direction has been replaced by the 0.1 % cross-coupling and f_v is the resonant frequency of the vertical suspension mode.

4.2 Suspension Upgrades

A reduction in suspension thermal noise can be attained either by reducing the temperature of the detector and/or directly reducing the mechanical loss. The upgrade proposed by the Strawman Red team retains a room temperature detector and thus aims to lower the mechanical loss. In principle an easy way to achieve this



Name	Mass (kg)	L (m)	Stock Diameter (mm)	Stock Length (mm)	Neck Length (mm)
aLIGO	40	0.6	3	11	7
Option #1	40	1.2	5	5	2
Option #2	160	1.2	5	5	2

Table 2: Parameters used to estimate the performance improvement in the LIGO-3 suspension

improvement is by increasing the dissipation dilution of the suspension. For an ideal suspension of diameter, d , and cross sectional moment, $I = \pi d^4 / 64$, the dissipation dilution is [12]

$$D = \frac{L}{1} \sqrt{\frac{mg}{YI}} \tag{3}$$

where L is the length of the suspension, m is the mass and g is the local acceleration due to gravity. An ideal suspension assumes that the fibre transitions from its thin section to an infinitely rigid section and thus all the bending energy is located within the fibre. Although a real fibre tapers via a neck and must be analysed with FEA, such an ideal fibre is useful in demonstrating that an increase in the suspension length is a fairly simple way to improve dilution. Figure 3 shows a scaled drawing of the available envelope within a BSC and suggests that an increase in the length of the monolithic stage from the current value of 60 cm to approximately 120 cm is possible (further extension to the suspension length would require an expansion flange in the BSC chamber). The increased suspension length will require that the ISI and QUAD are installed separately (i.e not as a cartridge installation) although this is not likely to be a major design driver. Additional methods to further improve the dilution involve utilizing a thicker stock from which the fibre is pulled, pulling with a shorter neck section, and shortening the neck length of the fibre. All three of these modifications reduce the energy leakage up the fibre and thus reduce effects associated with non-cancelled thermoelastic loss and weld loss. For aLIGO and the LIGO-3 upgrade the following fibre parameters in table 2 are assumed.

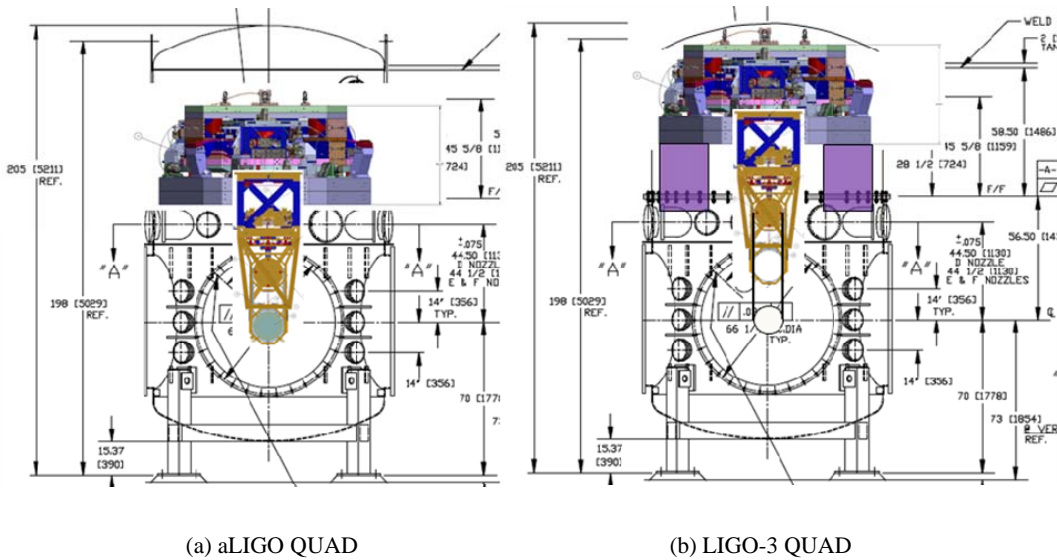


Figure 3: Available space within the BSC vacuum enclosure for (a) the aLIGO baseline (b) the proposed LIGO-3 upgrade

A second improvement can be achieved by directly reducing the mechanical dissipation in the weld/fibre. In aLIGO the fibre geometry will be chosen such that the thermoelastic contribution is nulled, leaving surface loss and weld loss as the dominant terms with roughly equal contributions. Previous measurements of the surface



loss in fused silica fibres [7, 8, 13, 14] provide data which spans a variety of fibre diameters from 50 μm to 400 μm . Furthermore there is some evidence that surface treatments have lowered the mechanical loss. In Ref [13] a series of heat treatments (from 20°C – 330°C) were applied to the fibres with the lowest mechanical loss observed at 60°C. The observed reduction was approximately a factor of 2 and was attributed to a reduction in water adsorption on the surface of the fused silica. There is little data on the origin of weld loss in fused silica fibres. A programme of R&D is underway in Glasgow and it is believed that thermal stress in the weld region is an important factor.

For the purpose of this document, and to make a conservative estimate of the performance gain, the noise models do not assume any improvement through a reduction in either the surface loss or weld loss. However, to give an idea of the potential improvement, a reduction in the thermal noise by $\simeq 15\%$ could be possible by reducing both the surface and weld loss by a factor of 2 for suspensions with 40kg masses (e.g aLIGO baseline or longer suspension options). For heavier mass options (e.g 160 kg) the importance of non-nulled thermoelastic loss becomes more important as the heavy mass pushes more bending energy into the thicker end of the fibre stock. In such cases a reduction in the surface and weld loss by a factor of 2 could lead to a reduction in the thermal noise by $\simeq 7\%$. It should be emphasised that in order to model the realistic thermal noise improvement, a full Finite Element model must be performed, and the final benefit of these enhancements depends on the level of surface/weld loss to non-cancelled thermoelastic loss in the fibre neck. This is highly dependent on the geometry of the fibre neck and stock length.

The test mass value is clearly an important variable in the LIGO-3 upgrade. In order to reduce radiation pressure noise a heavier test mass is clearly desirable. Values of 160kg are considered optimum and this increased payload needs to be carefully considered in terms of thermal noise performance, carrying capacity of the BSC/ISI and the local control authority of the QUAD. It is fairly simple to model the effect of the thermal noise from the heavier test mass and for this reason we consider (i) Option #1 which is a 1.2m long 40kg suspension (ii) Option#2 which is a 1.2 m long 160 kg suspension. For each option the fibre diameter is modified in order to maintain the static stress necessary to null the thermoelastic contribution. For Option#1 the thermoelastic cancellation region (the end 20 mm of the fibre where the bending occurs) has a diameter of 800 μm while Option#2 has a diameter of 1624 μm . Following the aLIGO design, the remaining thin section of the fibre is reduced in diameter (283 μm /566 μm for Options #1/#2 respectively) in order to increase the violin mode frequency. In this case the static stress in the fibre is increased from 0.78 GPa (aLIGO) to 1.56 GPa in order to ensure that the violin modes are >350 Hz for the longer suspensions. Further R&D will be performed to assess the practicality of this modification although fibres display strengths up to 5 GPa.

Although Option #1 will be a much simpler refit into the aLIGO vacuum enclosure it is worth noting the steps necessary to incorporate a heavier test mass. The aLIGO QUAD main/reaction chain has a total mass of 248kg with mass values for the upper/intermediate/penultimate/test mass of 22/22/40/40kg respectively. Simply increasing all masses by a factor of 4 would result in a payload 992kg. This is likely to be close to the limit of the capacity of the BSC piers and the ISI, given the fact that payloads are often not centred and therefore require balance masses and/or folding mirror suspensions. Any reduction of the total payload is clearly desirable. It is possible to lower the total payload by keeping the reaction chain identical to the aLIGO design and reducing the upper masses in the main chain. Maintaining the reaction chain masses will require a larger control force from the local control actuators and will result in a reaction chain displacement up to a factor of $10\times$ the aLIGO value ($\simeq 10^{-17}$ m). This will pose no problem for the actuators which will remain linear throughout this extended range. The main chain masses of the aLIGO QUAD pendulum are chosen such that there is good modal coupling between the upper masses and lower masses for local damping. Reducing the upper mass values will reduce the effectiveness of this local damping but may be an acceptable compromise. For example, utilising an upgraded QUAD with mass values 44/66/120/160 kg and a standard aLIGO reaction chain of 22/22/40/40 kg will only increase the payload to 534 kg. In order to achieve a lighter penultimate mass it is assumed that both the penultimate and test mass have a diameter of 55 cm and a thickness of 23 cm and 30 cm respectively. Further work is ongoing to explore the full range of payload configurations with a modified version of the aLIGO Mathematica Model.



4.3 Performance benefit of the upgrades

The following models have been run to provide the seismic noise and suspension thermal noise comparisons to the aLIGO baseline;

- A QUAD Mathematica model with modified parameters to reflect the new suspensions. For Option #1 this includes main chain masses of (21kg/21kg/40kg/40kg) and a longer final stage. For Option #2 this includes heavier masses (44kg/66kg/120kg/160kg), a longer final stage, thicker metal wires and thicker cantilever springs to support the increased payload, and modified wire attachment points to maintain a stable suspension. In these models the lower silica stage was 'turned off' by multiplying the silica fibre loss terms by a factor of 10^{-4} . The output of the models are (i) a transfer function which is used together with the baseline ISI performance (2×10^{-13} m/ $\sqrt{\text{Hz}}$ at 10 Hz and falling as $1/f^{2.7}$) to generate the seismic noise performance (ii) a set of vertical and horizontal thermal noise terms originating from the cantilever springs and metal wires.
- ANSYS Finite Element models for the 1.2 m long suspensions with test mass values of 40 kg (Option #1) and 160kg (Option #2). An initial figure of merit for each suspension is obtained from the dissipation dilution which is 110/220/50 for aLIGO/Option #1/Option #2 respectively. The improvement in the Option #1 dilution results both from the thicker fibre stock and the longer suspension. The heavier mass for Option #2 reduces the dilution value as more bending energy is stored in the neck region of the fibre. At the current time only the horizontal thermal noise has been calculated from the Finite Element model. For the purpose of this document it is assumed that the horizontal and vertical thermal noise contributions are equal (i.e. the total thermal noise is $\sqrt{2}$ times larger than the horizontal thermal noise alone). This is a reasonably conservative assumption and further modelling will follow to generate the full noise curve.

The output of the Mathematica model and the ANSYS model were added in quadrature to produce the final strain sensitivity curves plotted in figure 4 for the aLIGO baseline, Option #1 and Option #2. At 10 Hz the seismic noise is a factor of 2/1.5 lower than the aLIGO baseline for Option #1/#2 respectively, due to the lower resonant frequency of the longer suspension. Additional work is currently underway to optimise the value of the suspension break-off points for Option #2 in order to lower the transfer function to a similar level as Option #1. The suspension thermal noise is a factor of 4.5/4.5 lower than the aLIGO baseline at 10 Hz for Option #1/#2 respectively. This is a significant performance gain for upgrades which are based on sound engineering. The different shape of the thermal noise curve for the longer suspension options results from the 40 kg/160 kg payloads, which leads to different contributions from thermoelastic, surface and weld loss. At frequencies around 10 Hz the thermal noise originating from the metal cantilever blade springs is only a factor of 1.2/1.3/1.5 (aLIGO/Option #1/Option #2 respectively) lower than the thermal noise originating from the silica stage. To push this noise lower would require further R&D on the manufacture of the final stage springs from an alternative material such as fused silica. Methods to fabricate springs with high strength (>780 MPa) and make them tolerant to handling is clearly an important area of further work.

In summary, fairly modest changes to the suspension geometry can provide significant improvements to the seismic noise and suspension thermal noise performance. The violin modes are pushed up to approximately 350 Hz by operating the silica fibres at a higher stress level while the suspension bounce mode lowers to 4.4 Hz. Two payload configurations have been considered (i) a standard aLIGO version with 40 kg test mass (ii) a heavier 160 kg version in order to reduce radiation pressure noise. The latter option assumes a re-configuration of the QUAD payload (e.g., an aLIGO reaction chain and a 44kg/66kg/120kg/160kg main chain) in order to maintain a workable value for the ISI and BSC support piers.

4.4 Research plan towards reducing suspension thermal noise in LIGO-3

There are a number of areas which require further R&D:

- Utilising the full space within the BSC envelope requires the lifting the entire ISI and QUAD pendulum by approximately 75 cm. Finite Element analysis needs to be performed in order to ensure that a suitably

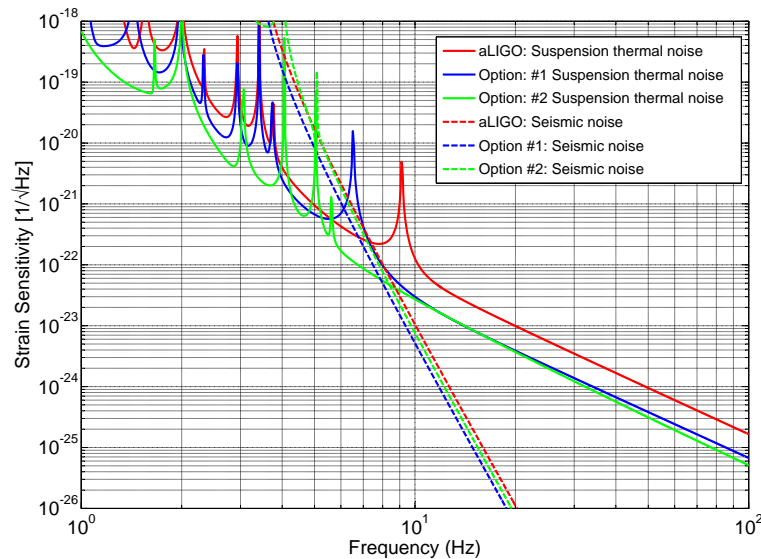


Figure 4: Comparison of strain sensitivity for the aLIGO baseline and the Option # 2 incremental upgrade

stiff structure can be fabricated which has high resonant modes (>100 Hz). A longer suspension will also require a change to the cartridge installation procedure.

- The techniques necessary to pull and weld 5 mm diameter fused silica fibres with sufficiently short neck and stock needs to be further developed. Initial tests appear promising but suitable tooling and an extension to the pulling machine need to be proven. Furthermore, the possibility of using a factor of 2 higher stress in the fibres must be fully assessed and the parameter space explored with 40kg metal test suspensions.
- Further Finite Element Analysis needs to be performed on the final stage of the suspension to assess the contribution from the vertical thermal noise.
- Additional work is needed to optimise the mass values of the QUAD main chain and reaction chain. For the purpose of this work the reaction chain is assumed to remain identical to the aLIGO baseline while the main chain has increased in mass. The effect on local damping, d -values, resonant modes and control authority needs to be fully investigated through the aLIGO Mathematica model.
- Fused silica cantilever springs will reduce vertical thermal noise well below the horizontal contribution. In order to achieve this performance gain requires the development of high tensile strength springs, which are suitably robust to handling, and the provision of attachment points to metal/glass interfaces.
- The use of improved BOSEM sensors (e.g., the EUCLID interferometric device) needs to be fully assessed for reducing sensing noise in the QUAD pendulum.
- Methods to characterise and potentially reduce fused silica surface loss and weld loss need to be investigated and further demonstrated.
- A re-design needs to be performed on the QUAD hardware such as interface plates, metal masses, wire jigs, cantilever springs and catcher structures.



5 Newtonian Noise

5.1 Introduction

In the context of gravitational wave interferometers, Newtonian noise (NN) refers to the fluctuation in the local gravitational field at the test masses. Differential motion of test masses caused in this way will couple into the gravitational wave channel as ‘Newtonian’ noise. It is useful to make the distinction at this point that we do not consider static spatial gravity gradients as a noise source³. Current estimates suggest that NN may become a limiting noise source in LIGO-3. As part of the LIGO-3 strawman exercise we therefore seek to collate the current knowledge on this topic and to apply it specifically to the LIGO sites. This will involve making predictions for the NN spectra at the two sites based on the seismic spectra, and outlining a potential future research plan towards NN reduction. We will also consider some more ‘outside the box’ ideas. In the absence of any experimental demonstration of NN cancellation, we put forward a rough estimate for the level of cancellation that may be achievable in the LIGO-3 interferometers.

5.2 Current best estimates of Newtonian noise

Estimates have been made within the gravitational wave community for Newtonian noise from a number of sources. These include anthropogenic [15], atmospheric [16], and seismic [17], [18] sources. The most troubling contribution is expected to be from seismically driven NN, so this is the source which we will mainly consider in this note.

The curve for NN that is currently on the Red Team strawman sensitivity curve is obtained using measured seismic data at the Livingston site, available in [19]. This data set contains seismometer displacement spectra in x, y and z directions, for a range of percentiles. The naming convention for these percentiles is that for the Xth percentile, the noise is lower than the stated level for X% of the time. The relevant seismic spectrum is calculated in the function `RealSeismic.m` by adding in quadrature the seismometer spectra for x, y and z components for a given percentile. The data is interpolated over to return values for the frequency range specified in the main `gwinc.m` function. The value of data points above about 100 Hz is set to an arbitrary low value of 10^{-13} m/ $\sqrt{\text{Hz}}$. The function `gravg.m` is used to calculate the NN contribution from the interpolated seismic data.

Some important things to note for this current calculation are:

- The seismic data is from LLO only.
- The current NN plot is calculated from seismometer data at the ETMX station.
- The 90th percentile is currently shown.
- A subtraction factor of 5 is assumed currently. This estimate comes from the fact that the seismically driven NN level is expected to be around a factor of 5 above the level of the other NN sources, such as the vibrations of the building itself (see figure 5). In order to get more than a factor of 5 subtraction of NN, it would be necessary to accurately measure the motion of these additional sources. For this reason we assume the cautious estimate that we can just subtract the seismically driven NN, resulting in roughly a factor 5 reduction in total NN.

³The term ‘gravity gradient noise’ could potentially lead to some confusion since the term ‘gravity gradient’ is commonly used to describe the spatial derivatives of the gravitational field. We use the term NN instead to avoid confusion.

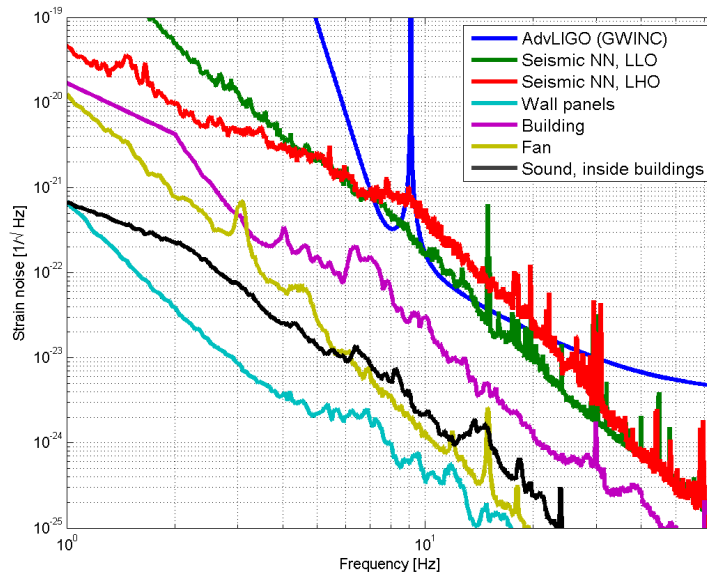


Figure 5: Estimates for contributions to the NN spectra at the LIGO sites as reported in [20]. Seismically driven NN is expected to be the dominant contribution to the overall NN level. It is important to note that the NN curves reported here are higher than the one assumed in figure 2 e.g., about a factor 10 at 10 Hz: this is due to the already mentioned subtraction factor 5 assumed for LIGO-3 and to the specific location considered to derive the seismic noise curve - ETMX at LLO, usually quieter than others.

5.3 NN mitigation techniques

5.3.1 Seismic shielding

Although it is not possible to shield the test masses themselves from the local gravitational field, it may be possible to shield the sites themselves from the action of seismic waves, especially the Rayleigh surface waves, which are expected to be the most harmful in terms of NN. As originally suggested in [17], one might consider a ‘tidal barrage’ like arrangement of concrete filled shafts surrounding the site, arranged at spacings equal to one quarter of the most harmful seismic wavelengths. Such an arrangement could possibly afford the site an effective shielding from seismic waves. A study into the feasibility of engineering such a structure at the sites should be made. The necessary physical size and composition of the shafts is expected to be a major influence on the viability of this option, and so should be estimated.

A version of a 2D FDTD Matlab simulation for seismic waves was found [21] and used to see how structures in the ground could deflect incoming seismic waves. A linear structure was tested consisting of 40×40 m holes spaced 80 m apart over ≈ 1 km. As the simulation is limited to 2D the holes are effectively infinitely deep. In reality as we are interested in attenuating surface waves, these holes might only have to be ≈ 100 m in depth. Since the depth of the holes might be crucial factor in evaluating the feasibility of this plan, this figure should perhaps be investigated further. The material chosen for the ground was Basalt rock, whose average density was $\approx 3 \times 10^3 \text{kgm}^{-3}$, the holes are considered to be made of air. The resolution of the simulation was set to 40 m thus the structures are one ‘pixel’ in size⁴. A plane seismic pressure wave was aimed at the structure and the result plotted.

This type of structure would only be a solution if one particular frequency of seismic wave was dominating the NN spectrum. Also, such a structure will only perform optimally if the seismic waves are incident at the

⁴It is worth noting that, for typical speed of seismic waves, about 200 m/s, the optimal barrage size for seismic waves around 10 Hz would be $\lambda_4(10\text{Hz}) = \frac{200\text{m/s}}{4 \times 10\text{Hz}} = 5$ m.



detector site from a particular direction: the linear structure must be built perpendicular to the propagation direction of the wave. One such possible source might be seismic waves generated by the ocean.

The plots in figure 6 show how a seismic wavelenths of 350 m, 700 m and 1400 m interact with the linear structure. As can be seen a wake effect is present behind the structure where we see the seismic wave is attenuated by roughly a factor of 0.5.

It is important to stress here that tidal barrages are likely to be much less effective either in the high frequency range - where seismic sources are often very close to the test masses - and for very low frequency waves - where the large optimal barrage size required to block the long seismic wavelengths can't be achieved for practical reasons. Further investigations are therefore required.

Furthermore, building such a structure would be a huge undertaking and would result in a lot of seismic noise from construction for many months, if not years. It would have to be known that such a structure would not only be necessary but actually work as the cost and time effort would be considerable.

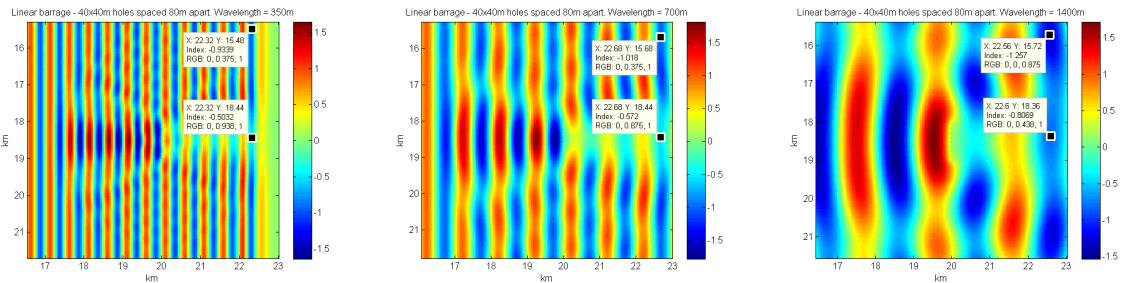


Figure 6: The results of 2D finite-difference time-domain simulations of the effect of a 'seismic barrage' on reducing the amplitude of seismic waves at a specific location. Left: barrage simulation for wavelengths of 350 m. Center: wavelengths of 700 m Right: wavelengths of 1400 m.

5.3.2 Coherent noise subtraction using seismometer array data

The most promising technique for NN mitigation is to use an array of seismometers to collect data about the motion of the ground in the vicinity of the test masses and either use this to cancel the NN online or offline [22], [23]. Assuming that the motion of the ground near the test masses is coherent with the gravitational potential experienced at the test mass, some cancellation of the effects of NN should be possible. The level of subtraction that is possible is not yet known accurately, but can be expected to be limited by the coherence between the seismometer signal and the NN, and also potentially by the sensitivity of the seismometers themselves. One possibility is to use an adaptive filtering, technique to find a combination of signals from the seismometer array that performs best in reducing the level of NN in the gravitational wave channel of the interferometer. This technique might not in fact require detailed knowledge of the surrounding bedrock composition and environmental factors, since the adaptive filter should effectively accommodate for this. Any scattering of the seismic waves that occurs between the seismometers in the array and the test masses themselves will significantly impact the coherence between the signals however, and will likely therefore limit the level of cancellation that is possible. Some work has been done within the community towards evaluating the effect of scattering of seismic waves on the effectiveness of NN cancellation [22].

We propose that a detailed study of the seismic environment at the LIGO sites will be necessary in advance of any implementation in any case, in order to more accurately assess the level of coherence between signals that we can expect, and thus to estimate the level of subtraction that might be achievable. Current estimates put the achievable level of subtraction with this method at around a factor of 5.

Time dependence in the coherence between seismic array signals and the NN in the detector may limit the efficiency of online (feed-forward) subtraction. If only offline subtraction is possible, this will not be of much help for the low latency pipelines, and could therefore delay the triggering of EM follow up searches.



5.4 Research plan towards reducing Newtonian noise in LIGO-3

There already exists a note from Jan Harms on the DCC which outlines a potential plan for moving forward with NN analysis at the LIGO sites [24]. In this note an experimental plan towards evaluating the correlations in noise from various sources is presented. One outcome of this work would be to decide whether or not Newtonian noise from the walls, ceiling and atmospheric sound noise from outside the buildings can be disregarded. Also the detailed understanding of correlations between ground motion around the test masses will inform the configuration of a seismic array. In this study we aim to extend the research plan to include simulations for estimating the maximum possible subtraction with a given level of correlation and a given seismometer array, and table-top experiments for validating the methods of cancellation.

5.4.1 Simulations of Newtonian noise and its cancellation at the LIGO sites

Although a lot of work has been done towards evaluating the seismically driven NN in underground locations, and the likely achievable cancellation there [18], [25], the same data is not yet available for the LIGO sites. The measurements proposed in [24] will be very useful for reconstructing the seismic field around the detector site. Simulations should be performed to estimate the coherence between seismometer measurements and the GGN present in the GW channel of the interferometers. A possible plan to this end might be as follows:

- Make a 3D model of the geology around the sites. The data collected from the measurements referred to in [26] will be very useful for this.
- Using perhaps a Monte-Carlo method, compute a likely pressure/ density wave spectrum within the rock that could give rise to the observed seismic spectrum at the surface. The data mentioned in item one will be essential in determining the transfer function from density perturbations in the rock to acceleration measurements at the surface. Data collected from the experiments described in [24] will also be very useful here.
- With this estimated density perturbation spectrum we can estimate the NN spectrum at the test mass locations.
- Since we also in principle know the transfer function from density perturbations to the seismometer signals, we can estimate the maximum correlation between the seismometer signals and the NN as it appears in the gravitational wave channel. Finite-difference time-domain simulations may prove more useful than frequency domain calculations using spectra here.

It is clear that strong communication with the DetChar group will be invaluable in this exercise, as they have the most information about the site specific environmental factors. One aspect to consider might be the different sources of NN at different characteristic frequencies. If, for example, wind shaking the building is found to often make the level of NN from movement of the walls or ceiling level worth considering, we should look at potential ways for reducing this effect, such as 'streamlining' the buildings. There may be other such considerations very specific to the site which communication with DetChar may reveal.

5.4.2 Experimental investigation of accelerometer array based noise cancellation

In order to validate theoretical predictions for the level of noise cancellation that is possible with a seismometer array it will be necessary to perform table-top experiments. We envisage a table top investigation into the effects of surface inhomogeneities on the coherence between accelerometer measurements and either the generating source signal and/or signals from an interferometer on the surface in question. It is clear that we will not be able to set up a table-top system that is sensitive to actual NN. We might therefore wish to use an analogue to the NN in an experiment.



6 Coating Brownian

6.1 Overview

The power spectral density of the coating thermal noise is typically estimated using the following formula [27]:

$$S_x(f)_{\text{coating}} = \frac{2k_B T}{\pi^2 f Y} \frac{d}{w_0^2} \left(\frac{Y'}{Y} + \frac{Y}{Y'} \right) \phi_{\text{coating}}, \quad (4)$$

where f is the frequency in Hz, T is the temperature in Kelvin, Y is the Young's modulus of the substrate, Y' the Young's modulus of the coating, ϕ_{coating} is the mechanical loss of the coating, d is the coating thickness and w_0 is the laser beam radius.

The Advanced LIGO mirror coating design uses titania-doped tantala (loss $\approx 2 \times 10^{-4}$) as the high-index material and silica (loss $\approx 0.5 \times 10^{-4}$) as the low-index material. A standard highly-reflective coating uses multiple alternating layers of high-index and low-index materials, with the thickness of each layer chosen to be have an optical thickness of $\lambda/4$ at the wavelength to be reflected. The Advanced LIGO coating design is optimized so that the thickness of the lossy tantala layers is minimised, the thickness of the silica layers is increased and the total number of layers adjusted to maintain the required reflectivity. This optimization process can reduce the coating thermal noise by a factor of $\approx 10\%$ [28].

There are several potential strategies for reducing coating thermal noise. Perhaps the most intuitive method is to reduce the temperature of the mirror. However, both silica and tantala have loss peaks at cryogenic temperature [29, 30], which may significantly reduce the thermal noise benefits of cooling these coating materials. Current estimates based on the measured loss of single layers of silica and tantala suggest that cooling to 20 K would only reduce the coating thermal displacement noise by a factor of ≈ 1.7 , rather than the factor of 4 which could be achieved if the coating loss was independent of temperature. The use of cryogenic cooling would also require significant alterations to the Advanced LIGO infrastructure, possibly including a change of the mirror substrate material as the loss of fused silica increases from $\sim 1 \times 10^{-9}$ at room temperature to $\sim 1 \times 10^{-3}$ at 30-50 K. However, if the mirror substrate material were to be changed (e.g., to silicon), then cryogenic cooling could be used to reduce thermal noise, perhaps using alternative coating materials with a lower mechanical loss than tantala at low temperature.

In this document, we consider several methods of reducing coating thermal noise. The first of these is to increase the laser beam radius, so that the thermal noise is effectively averaged over a larger area. While this would involve some technical changes to the Advanced LIGO infrastructure (i.e. larger mirrors), the dependence of coating thermal noise on the beam radius is well-known, and the suggested increase in beam diameter would be reliably expected to reduce the thermal displacement noise by a factor of 1.6. This is discussed in more detail in section 6.2.

In addition to this, we discuss three additional approaches which may be used in conjunction with a larger beam radius to further reduce coating thermal noise. These approaches are: the use of waveguide optics to reduce the thickness of coating that is required (see 6.6), the use of alternative multi-layer coatings (see 6.5) and the use of Kahlili cavities (see 6.3). We estimate that each of these methods could potentially reduce coating thermal noise by at least an additional factor of 2.

6.2 Increasing the beam size

In order to reduce the coating Brownian noise contribution we consider an increase of the laser beam radius on the main arm cavity mirrors of 1.6 compared to the advanced LIGO baseline. The required changes of the radius of curvature of the mirrors and the corresponding laser beam radii are shown in Table 3. While the beam radius at the input mirrors will increase to 8.46 cm the largest beam radius will occur at the end mirrors with nearly 10 cm. In order to keep the clipping losses below 1 ppm we have to increase the mirror diameter accordingly by a factor 1.6. Increasing the main mirrors, while keeping the aspect ratio constant will increase



the mirror mass by about a factor of 4 to 160 kg, which as we will see in Section 7, is also quite beneficial to reduce quantum radiation pressure noise.

Table 3: Mirror curvatures and beam sizes in the arm cavities

Parameter	Advanced LIGO	Strawman Red Design
ROC of ITM [m]	1934	1849
ROC of ETM [m]	2245	2173
cavity length [m]	3996	3996
spot size at ITM [cm]	5.31	8.46
spot size at ETM [cm]	6.21	9.95
mirror diameter [cm]	34	55
waist position [m]	1835	1835
waist size [cm]	1.20	0.74
g-factor of arm cavity	0.832	0.974

Usually the maximum feasible beam size is limited by the size of the vacuum tubes, by the available substrate size, by the stability of the cavities (g-factor $\rightarrow 1$) or by any combination of the three. With a clear aperture of the LIGO vacuum tubes of 1 m (and assuming that only a single interferometer will be housed in the Hanford envelope) the tube size is not a limiting factor. Also the substrate size is not a problem as Suprasil 3002 (input mirror material) and Suprasil 312 (end mirror material) are already now available in the required diameter and mass.

For our design the most critical aspect of the increased beam size is the reduced stability of the arm cavity. The proposed coating Brownian noise improvement of 1.6 would require to push the arm cavity g-factor up from 0.832 to 0.974. This will impose significantly stricter requirements for the thermal compensation systems as well as for the surface quality of the mirrors. One of the main R&D tasks regarding coating Brownian noise will be to find out what the largest beam size for robust operation of LIGO3 will be. The experience that will be collected during the commissioning of Advanced LIGO, combined with numerical simulations, will be a crucial input to this task.

Finally, we need to consider that increasing the beam size in the arm cavities will also require a larger beam splitter and a redesign of the telescopes inside the non-degenerate recycling cavities. Though no significant challenge, these two points will cause additional effort and cost.

6.3 Khalili cavities

Coating Brownian noise is dominated by the mechanical losses in the Ta₂O₅ layers of the dielectric coating. Doping the Ta₂O₅ with TiO₂, optimising the coating process, and minimising the thickness of the Ta₂O₅ layers yielded an improvement in coating Brownian thermal noise, which is already included in the sensitivity curve of the aLIGO design. Further improvement in coating Brownian noise requires a reduction of the mechanical losses in the coating or reducing the influence of inevitable mechanical losses on the detector sensitivity. The usage of Khalili cavities aims for the latter approach. In his paper in 2005 Khalili showed that coating thermal noise can be reduced by replacing an end mirror with a short Fabry Perot cavity [31]. In this proposal the reflecting dielectric layers are distributed onto two substrate surfaces, forming an anti-resonant optical cavity (see middle part of figure 8). While the displacement (induced by thermal noise) of the dielectric coating of the first substrate fully couples to the noise at the output of the interferometer, the coupling of a displacement of the dielectric coating of the second substrate is reduced. A similar reduction effect can be achieved by distributing the dielectric coating onto the front and rear surfaces of a single substrate thus forming an etalon (see right part of figure 8). The pros and cons of Khalili cavities vs Khalili etalons are described in [32]. In this paper the gain in coating thermal noise for advanced LIGO has been estimated to a factor of two, which is the suppression factor that we assume in this proposal. The gain is (for very thick mirrors as considered for Strawman Red)

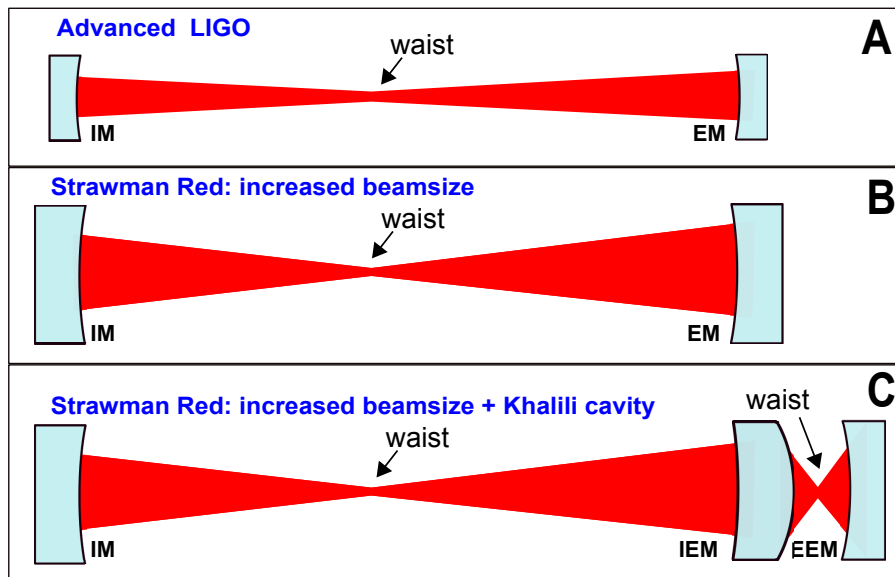


Figure 7: Simplified schematic of the arm cavity geometry of Advanced LIGO (A), the Strawman Red design featuring 160 kg mirrors and a beam size increased by a factor 1.6 (B). The additional use of anti-resonant end mirror cavities (so-called ‘Khalili-cavities’) as shown in (C) allows to further decrease the total coating Brownian noise by a factor 2. In order to achieve non-degeneracy in the Khalili cavity the IEM substrate features a lens with a focal length of half the length of the Khalili cavity.

nearly independent on whether cavities or etalons are used. The choice between Khalili cavity and Khalili etalon is driven by technical and financial aspects.

While a Khalili etalon requires considerably less hardware (only one substrate and suspension, no additional vacuum tanks and no additional beam tube) the requirements in terms of thermal lensing compensation are extremely demanding. Due to the shortness (lack of Gouy phase) of the Khalili etalon it is not possible to create an optically stable resonator. It is always on the verge to instability. Longitudinal and angular control of the etalon as well as compensation of the thermal lens created by residual absorption will have to be done with thermal actuation. It is currently not clear whether and if so how this can be achieved with the required bandwidth and accuracy. For this reason we will assume the usage of Khalili cavities here.

In contrast, a Khalili cavity with a length of some 10 m (we will assume 50 m here) can be made optically stable by using the AR coated, rear surface of the first substrate as a lens, and this way gaining some Gouy phase in the Khalili cavity, as shown in figure 7. As a rough starting value for costing we assume a mirror separation of 50 m and a focal length of the lens on the order of 25 m. These values still needs to be optimized. The specification requirements for the surfaces in the Khalili cavity still need to be evaluated. For costing purposes we assume full main mirror costs here. Due to the physical properties of fused silica it is expected that the dependence of the refractive index on the temperature (inside the first substrate) has the dominating influence on the thermal lensing in comparison to thermal deformation of all surfaces involved. Details of the optical layout and the influence of the thermal lens still need to be investigated. In a trade off of performance vs costs, the manufacturing tolerances, thermal compensation system requirements, and control system aspects have to be balanced against the (minor) costs of added length for the beam tube.

Error signals for control purposes (longitudinal and angular) would presumably be done with the help of RF sidebands on lasers injected from the far ends, as also foreseen for the arm cavity locking of aLIGO. The length of a cavity, allows the easy usage of resonant RF sidebands in the low MHz range in contrast to a Khalili etalon which would require close to 1 GHz frequencies.

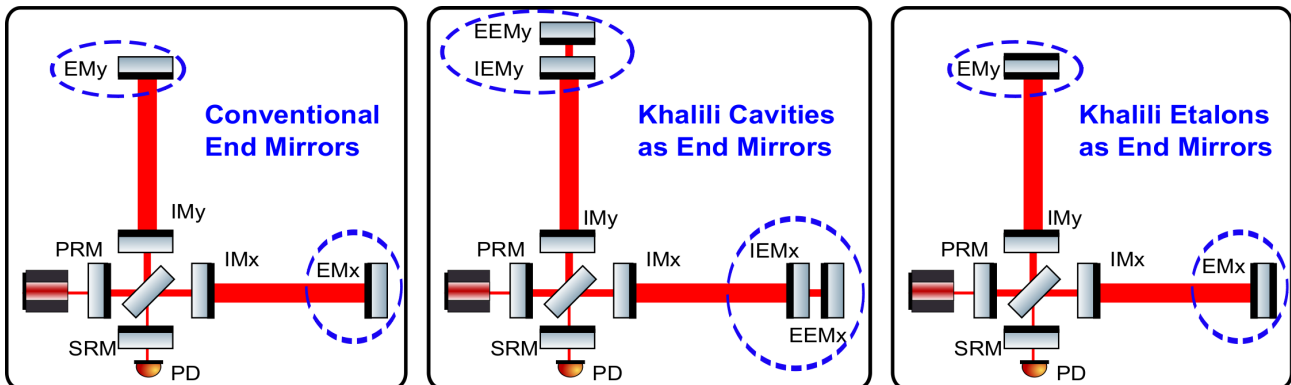


Figure 8: Simplified schematic of an Advanced LIGO interferometer with conventional end mirrors, featuring all the coating layers on their front (left), with Khalili cavities as end mirrors (center) and with Khalili etalons, featuring only a few coating layers on the front surface and the majority of the coating layers on the rear surface (right).

6.4 Required Hardware for Khalili cavities

The hardware requirements for the realisation of Khalili cavities at the ends of the interferometer arms as shown in the middle graphic of figure 8 is dominated by the addition of 50 m beam tube for each interferometer arm and an additional vacuum tank including a full seismic isolation and quad suspension in a separate building.

The required hardware is summarized in figure 9.

Khalili cavities require the following hardware:

- An additional building with all surrounding infrastructure. The footprint can be smaller than of the current and stations and has to be balanced against costs.
- 50 m of beam tube incl. baffles + enclosure.
- Two beam tube size gate valves.
- An additional vacuum tank of the same type (BSC) as in the current end stations (see list item 4).
- Active seismic isolation system.
- Two turbo molecular vacuum pumps + backing pumps + control units and monitoring equipment.
- Quadruple suspension of advanced LIGO type. The suspension performance for the EEM can be slightly worse than for the IEM at the ratio of suppression of displacement noise by the anti resonant Khalili cavity. This saves some costs.
- Mirror substrates, polishing and coating. We assume Suprasil 3002 to be used for the IEMs and Suprasil 312 for the EEMs, where no high power beam is traversing the substrate and homogeneity is less of an issue. Polish is assumed to be done conventional + ion beam figuring. Coating standard IBS + corrective coating if needed. AR coating on the rear surface of IEM.
- Khalili cavity control system

6.5 Optical coatings with reduced thermal noise

The use of suitable alternative mirror coatings may be the simplest method for reducing coating thermal noise as it would require no further modifications to the existing infrastructure. Thermal noise could be reduced by reducing the mechanical loss silica/tantala coatings by particular treatments (e.g., doping or heat-treatment), by

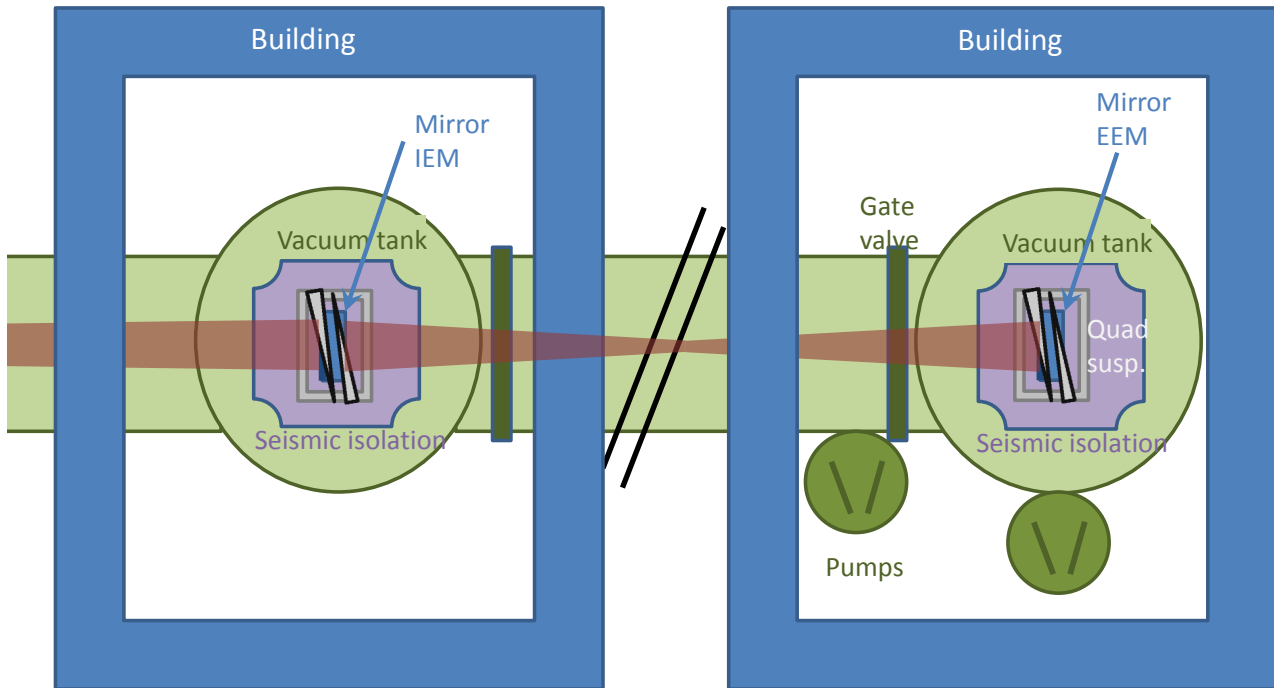


Figure 9: Schematics of the additional hardware required for the realization of Khalili cavities.

the development of alternative coating materials of lower mechanical loss or by using a coating with properties which allow the total coating thickness to be reduced. Significant research into reducing coating thermal noise is ongoing, and several promising avenues are detailed in the following sections.

6.5.1 Continued improvement of tantala coatings

The loss of tantala at room temperature can be reduced by approximately 40% by doping with titania [33]. Research aimed at developing detailed models of the loss mechanisms in tantala, and the mechanism by which doping reduces the loss, is ongoing. Measurements of cryogenic loss peaks in tantala have allowed characteristics of the microscopic mechanism responsible for the loss to be identified, and suggest that the loss is related to the local atomic structure of the material. Studies of the atomic structure using electron diffraction and novel semi-empirical amorphous modeling techniques have identified the first possible correlations between structural properties of tantala and the loss at room temperature. This is a highly active area of research and a detailed understanding of the relationship between loss and structure may allow methods of further reducing the loss to be developed.



6.5.2 High-temperature annealing of coatings

Post-deposition heat treatment is generally used to improve the optical properties of ion-beam sputtered coatings. Silica/tantala coatings are typically heat-treated at 500-600°C, and the tantala layers are known to crystallise, to the detriment of their optical properties, at temperatures between 600 and 700°C. However, there is evidence that the loss of silica coatings can be reduced by a factor of 2 by heat treatment at 900 - 1000°C [34]. Thus if tantala could be modified to prevent crystallisation, or if an alternative high-index material which can withstand higher heat-treatment temperatures could be identified, it may be possible to reduce the total coating loss through high-temperature heat treatments. Zirconia coatings are currently being studied within the LSC, and the use of several possible doping materials to attempt to prevent crystallization on heat-treatment is under investigation.

6.5.3 Amorphous silicon as a high-index coating material

Amorphous silicon is a possible alternative high-index material which has several attractive properties. It should be noted, however, that amorphous silicon is not transparent at 1064 nm, and thus would require a change of laser wavelength to e.g. 1550 nm. Previous measurements indicate that the mechanical loss of electron beam evaporated amorphous silicon coatings can be up to a factor of two lower than the loss of titania-doped tantala at room temperature ($\phi_{\text{coating}} = 1 \times 10^{-4}$) [35]. While e-beam coatings do not typically have the required optical properties, the fact that low losses have been measured in this material is promising, and measurements of the loss of ion-beam sputtered (IBS) amorphous silicon coatings are in progress.

The refractive index of amorphous silicon is significantly higher than that of tantala ($n \approx 3.5$ compared to $n \approx 2.01$). Thus for a standard quarter-wavelength coating design, the thickness of the high-index layers would be reduced from ≈ 131 nm to ≈ 112 nm by replacing tantala with amorphous silicon. Furthermore, due to the larger ratio of refractive indices ($n_{\text{high}}/n_{\text{low}}$) in a silicon/silica coating, the required reflectivity could be obtained with 6 bi-layers (compared to 15 bi-layers for a tantala/silica coating). Taken together, these factors give a total thickness of $2.2\mu\text{m}$ for silicon/silica, compared to $4.7\mu\text{m}$ for a tantala/silica coating. This reduction in thickness would result in a reduction of the thermal noise power spectral density by a factor of ≈ 2.1 .

If the mechanical loss of amorphous silicon is assumed to be 1×10^{-4} , the use of silicon/silica coatings would reduce the coating thermal noise power spectral density by a factor of ≈ 4.6 . If the coating layer thicknesses were optimised to minimise the total thickness of silicon while maintaining the total reflectivity, using the optimisation routines already developed for the Advanced LIGO coating, then a further reduction of the thermal noise would be expected. It should be noted that even if the mechanical loss of IBS silicon is found to be twice that of doped tantala, the use of silicon/silica coatings would still reduce the coating thermal noise power spectral density by a factor of 1.9, as the high refractive index of silicon reduces the required thickness of the coating.

6.5.4 Crystalline coatings

The use of epitaxially grown crystalline coatings may have some potential to reduce coating thermal noise [36]. Studies of an AlGaAs coating, in which the high-index and low-index layers are produced by varying the Ga content of the layer, have shown mechanical losses at room temperature as low as 2.5×10^{-5} . There are some things to be considered regarding crystalline AlGaAs coatings:

- AlGaAs coatings have to be grown on a GaAs crystal, for lattice matching reasons. This is typically done on a flat wafer (about $600\mu\text{m}$ thick), which is etched off the dielectric coating afterwards, which in turn is transferred to another substrate.
- While it is best if the initial wafer is flat (the curvature of an aLIGO test mass may be acceptable) the transfer can be made to a curved substrate. The bonding is often done involving liquids which are removed by heating.



- In order to allow this heating the thermal expansion coefficient of the dielectric stack and the substrate should match well enough (TBD).
- The mechanical losses of the bond are still unknown and need to be measured.
- In case of the ETM it is worth considering a GaAs substrate. The achievable minimal absorption at 1064 nm is not well known. The lowest values in the literature is 0.015/cm. (citation to be added). If the transmission of the ETMs is lowered to 1 ppm this may be acceptable but pose a problem for "green beam arm cavity locking" as the green absorption is much higher.

Crystalline mirror substrates are unlikely to be suitable for use at room-temperature due to high levels of thermoelastic loss. However, it is possible in principle to transfer a crystalline coating onto a new substrate. However, more research would be required into carrying out this process on the scale required and into the mechanical loss associated with attaching the coating to a fused silica test-mass. In addition, estimates of the level of coating thermoelastic loss arising from a crystalline coating on a fused silica substrate would be required.

An alternative crystalline coating can be made with alternating layers of GaP and AlP. These coatings can be grown on silicon substrates and investigations of the mechanical loss are underway.

6.6 Waveguide mirrors

One promising approach to significantly reduce the coating thickness is to use so-called resonant waveguide gratings (RWGs). These optical devices represent a fully alternative mirror concept with respect to conventional dielectric coatings. Their reflective function does not rely on multiple interference but on resonant coupling of incident light to a periodically nanostructured waveguide layer. Resonant waveguide gratings and its reflection phenomena have been first described in the early 1980s [37], followed by investigating their applicability as narrowband optical filters [38]. In 2006 Bunkowski *et al.* proposed their potential use as a low thermal noise alternative to conventional mirror coatings in gravitational wave detection [39]. Using the established material combination of fused silica/tantala and 1064 nm laser light they designed a grating structure comprising a thin (few hundred nanometers) but corrugated tantala layer on top of a fused silica substrate. In principle the reflectivity of such gratings reaches the same values as for conventional coatings.

Figure 10(a) helps to recall the working principle of RWGs in a ray picture and why they only need a thin high refractive index layer. Normally incident light hits the grating structure which has a subwavelength periodicity. This ensures that only the fundamental zeroth diffraction order exists in both air and the low refractive index fused silica substrate [39]. The grating periodicity has further to be chosen such that it generates the symmetric first diffraction orders in addition to the fundamental order in the high-index tantala layer. The first orders will then experience total internal reflection at the boundary to the substrate corresponding to the excitation of a laterally propagating waveguide mode. When hitting the grating again the higher diffraction orders will be partially reflected to remain in the waveguide mode but also partially diffracted to both the transmitted and the reflected zeroth diffraction order, see Fig. 10(a). If the grating structure is designed properly in terms of its geometric and material parameters all transmitted light can be prompted to interfere destructively corresponding to perfect back reflection.

Based on the design study in Ref. [39] tantala based waveguide mirrors have been fabricated and tested in table-top as well as prototype-scale interferometric experiments [40, 41]. Reflectivities of up to 99.2% and a stable operation of a fully suspended 10 m Fabry-Perot cavity could be demonstrated. A cross-sectional scanning electron microscope (SEM) image of such a fabricated and characterized tantala grating is shown in Fig. 10(b). The sample preparation for SEM characterization was done by using a focused ion beam (FIB) which requires covering the grating spot of interest by a platinum (Pt) layer. This image also shows the residual chromium (Cr) mask and a thin aluminum layer which are required for the fabrication process. Please note that the Pt as well as the Cr layer were not present on the characterized sample. From the image one can see that the effective coating thickness of such a tantala waveguide mirror can be as low as ≈ 250 nm while that of a conventional coating is about 6 μ m. Following Eq. (4) this suggests a remarkable Brownian noise reduction.

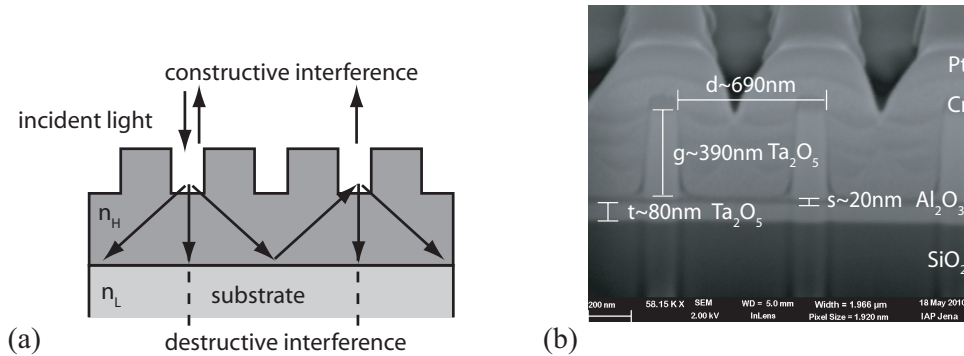


Figure 10: (a) Principle of a waveguide grating mirror under normal incidence in a ray picture. (b) SEM image of a fabricated tantalum waveguide grating structure. Both images taken from [40]

Taking into account also thermorefractive and thermoelastic noise, Fig. 11 shows the results of a preliminary simulation based noise estimation of tantalum based waveguide mirrors in comparison with a conventional Advanced LIGO coating [42]. The term 'preliminary' was chosen here since these simulations include several assumptions:

1. The material parameters such as the quality factor and thermal conductivity of the grating structure are assumed to be same (or at least similar) to that of a single layer material.
2. Effects due to a possible lateral expansion are not considered.
3. For coating stacks, the thermal diffusion length is assumed to be larger than the coating thickness. In case of RWGs this also has to hold for the lateral dimension which is not sure, due to the guidance of light in the waveguide layer.

In (a) the individual noise contributions are displayed while in (b) the incoherent sums of the three noise terms are plotted together with the substrate Brownian noise level as a reference. One can see that Brownian as well as thermoelastic noise of an RWG are significantly reduced compared to the coating stack simply due to the coating thickness reduction. However, thermorefractive noise is slightly increased which can easily be understood on a qualitative basis. Thermorefractive noise scales with the propagation length of light within the optical system. The light reflected from a typical quarterwavelength stack effectively senses only a few (≈ 6) double layers which corresponds to a penetration depth of about $1.5 \mu\text{m}$ and thus a propagation length of light in the coating of about $3 \mu\text{m}$. The propagation length l in a waveguide grating can be calculated from the bandwidth via Δf [43]:

$$l = \frac{\lambda \cdot d}{\pi} \cdot \frac{1}{\Delta f}, \quad (5)$$

with λ the wavelength and d the grating period. For a typical tantalum waveguide the bandwidth is 40 nm [39] which corresponds to a propagation length of $6 \mu\text{m}$. This doubled propagation length in a waveguide results in a doubled level of thermorefractive noise which is quite well reflected by the respective curves in the top graph of Fig. 11.

In total, the noise plots suggest a very promising reduction of coating thermal noise of tantalum RWGs by a factor of two compared to conventional coatings. By employing optimized grating designs thermorefractive noise of RWGs might even be improved down to the level of standard coatings. These encouraging results together with the experimental demonstrations bring tantalum RWGs into play as an interesting option for reducing the thermal noise of LIGO3. However, envisaging an actual application leaves very challenging exercises to be undertaken ranging from accessing the actual thermal noise level of RWGs to applying tantalum grating structures onto 160 kg fused silica substrates:

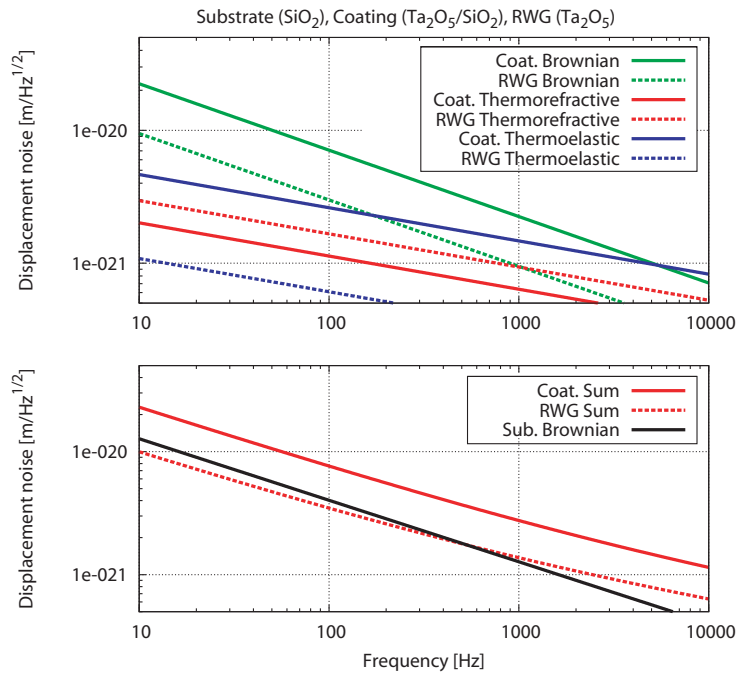


Figure 11: (a) Thermal noise estimates for a conventional multilayer stack and a resonant waveguide grating. While Brownian and thermoelastic coating noise for the stack are higher due to the larger amount of coating material, thermorefractive noise is significantly enhanced for resonant waveguide gratings. (b) Incoherent sum of the individual contributions in comparison with a fused silica substrate for a beam size of $r_0 = 0.062$ m (the ratio of coating and substrate thermal noise scales with $1/\sqrt{r_0}$). For this comparison it was assumed that material properties of a nanostructured layer are the same as for a single layer material. Plots taken from [42]

1. Access to the actual thermal noise level:
 - (a) Implementation of more realistic noise estimates
 - (b) Measurement of mechanical quality factors of thin nanostructured tantala layers
 - (c) Direct measurement of coating thermal noise of a tantala RWG
2. Increasing the reflectivity of tantala RWGs
 - (a) Investigation of more tolerant grating designs
 - (b) Measurement of RWG losses and absorption
 - (c) Characterization of scattered light
 - (d) Improvement of each fabrication step in terms of line edge roughness and grating parameter homogeneity
3. Fabrication of tantala gratings on 160 kg fused silica substrates
 - (a) Evaluation of different lithographic or imprint techniques with respect to the required substrate size and grating parameter homogeneity
 - (b) Evaluation of different etching techniques with respect to the required substrate size and grating parameter homogeneity



Dedicated research according to the first two bullet points is already on its way and the outcome of results is foreseen through the coming years. A greater challenge is driven by the intended use of 160 kg fused silica test masses with a diameter of 54 cm and a thickness of 32.4 cm. For grating fabrication referenced here, the lateral definition of parameters was done by electron beam lithography which is highly flexible as well as accurate and thus ideal for R&D. However, state-of-the-art electron beam facilities are not compatible with such proposed substrate dimensions and its weight. Existing techniques such as free-space holographic lithography or nano-imprint technology might be capable of overcoming this limitation and are more than worth taking into account. The same limitations apply to plasma etching chambers used so far, however, the gravitational wave community can benefit from the rapid progress in nanofabrication techniques which is driven by the semiconductor industry.

6.7 Alternative Beam Shapes

Using laser beams in the arm cavities with alternative beams shapes is another possibility of reducing thermal noise of the test masses. Since the original proposal discussed in Kip Thorne's research group at Caltech in 2000 a lot of related research has been undertaken in the gravitational wave community. [44] provides an in-depth, mostly analytical review on beam shaping and its prospects for reducing thermal noise and thermal effects. Initial work on so-called Mesa beams pioneered this topic and demonstrated the technology on a dedicated prototype [45]. Currently the performance of Mesa beams is limited by the requirement for the cavity mirror surfaces to have a special 'Mexican-hat' like profile while retaining the same low-loss properties in terms of optical scattering. More recently the feasibility of higher order Laguerre-Gauss (LG) beams has been investigated. LG beams can be used with standard spherical surfaces which would remove the main disadvantage of Mesa beams. However higher-order Gaussian modes are degenerate, or, in other words, there are multiple modes with the same order so that an optical cavity resonant for a higher order LG mode will also be resonant for other modes of the same order. This is not the case for the currently used fundamental mode, which is unique in its mode order. This degeneracy can lead to additional optical losses. The performance of the LG₃₃ beam was investigated using simulations of arm cavities, with Advanced LIGO mirror maps describing mirror surface distortions. It was found that mirror surface distortions significantly reduce the purity of LG₃₃ circulating in a cavity, with relatively large amplitudes of LG₂₅ and LG₄₁ in the cavities. Current state-of-the-art mirror surface quality would result in significant optical losses [46, 47]. These results are based on numerical simulations; an experimental evaluation is still progress.

Feasibility limits of alternative beams are related to mirror surface quality and the resulting optical losses. Like for the determination of the ideal beam size (see Section 6.2), a better understanding of optical surface effects on the laser beam towards improving the surface quality itself is an important R+D activity.

Based on the recent results we do not consider alternative beam shapes as an option in this design. However, if sufficient advances in the manufacturing and characterisation of mirror surfaces become available, alternative beam shapes remain a very interesting option, as they are compatible with the future instruments and could be implemented in further upgrades (by exchanging the mirrors).

7 Quantum noise

7.1 Introduction

There are various ways to decrease the quantum noise, at least in a specific frequency region:

- **Increasing the light power** inside the interferometer arms reduces the shot noise level inverse proportional to the squareroot of the optical power. However, at the same time the radiation pressure noise increases linear with the optical power circulating in the arm cavities. Therefore, and because it is currently unclear whether the thermal compensation systems will work at powers beyond 1 MW we do not consider any increase of the optical power inside the main interferometer in our design.



- The application of **heavier test masses** provides a reduced susceptibility to quantum radiation pressure noise. Our design assumes to enhance the test mass weight from about 42 kg to 160 kg which decrease the radiation pressure noise contribution by a factor of about 4.
- **Signal recycling** [48] allows the quantum noise contribution to be shaped to optimise the overall detector response. The signal recycling bandwidth and the signal recycling tuning (i.e. the frequency of maximum sensitivity) can be adjusted by means of the reflectivity and microscopic position of the signal recycling mirror [49]. For our design we try to achieve an optimal broadband sensitivity and have therefore chosen to keep the signal recycling parameters similar to Advanced LIGO baseline, i.e., using tuned signal recycling and a signal recycling mirror with a power transmittance of 20 %.
- One of the key technologies for the future reductions of quantum noise is the **injection of squeezed light states** [50]. Especially the injection of frequency dependent squeezed light [51] looks very promising and is expected to provide a broadband quantum noise reduction by a factor of a few. As will be described our design assumes a squeezing source providing 20 dB of squeezing which is converted to have frequency dependent squeezing angle by using the reflection at a 500 m filter cavity. When keeping the optical losses the squeezed light encounters below 10 % it can be possible to achieve a broadband quantum noise improvement of about a factor 3.
- Finally the quantum noise can also potentially be reduced by moving away from a standard Michelson interferometer. A multitude of quantum-non-demolition configurations has been suggested over the last two decades, including **optical rigidity** topologies [52–54] and **speed-meter** [55] configurations. Please note that these techniques might require a close-to-complete reorganisation of the interferometer configuration inside the vacuum facilities. Moreover, so far only very little experimental experience has been gained with such configurations. Therefore, we only mention non-Michelson configurations at the end of this section as alternative configurations that deserve further investigations and R&D efforts to fully evaluate their potential.

Section 7.2 describe the generation and injection of squeezed light and summarise the expected optical losses. The filter cavity required for the generation of frequency dependent input squeezing will then be described in Section 7.3. A brief list of the required hardware is then given in Section 7.4, before alternative interferometer topologies (speedmeter and local readout) are discussed in Section 7.5.

7.2 Squeezing generation, injection, and detection losses

In this section we will briefly review the estimated optical losses of the squeezing generation, injection, and detection path. Most of the quoted numbers are based on experience with the squeezing setup used in GEO 600, extended by assumptions of future developments.

7.2.1 Squeezing generation

Losses in the optical parametric amplifier (OPA) used to generate the squeezed vacuum states are currently about 4-5 %, dominated by losses inside the optical medium. Potentially this loss can be lowered, by lowering the finesse of the OPA cavity. A limit to this approach is set by the fact that with lower finesse, the bright beam, that is crucial for mode-matching and alignment of the squeezing beam to the IFO/filter cavity, will have less overlap with the squeezing mode beam. We assume for Strawman Red that 3 % loss in the generation of the squeezing can be achieved.⁵

⁵Recent work [56] has shown that even 2.5 % loss can be achieved, which would free up 0.5 % of the loss budget for other purposes, such as for instance the creation of alignment control signals.



7.2.2 Optical isolation and injection

One Faraday rotator (FR) and polarizing beam splitter (PBS) is needed in order to inject the squeezed vacuum onto the main IFO optical path. If another PBS is added, an additional reduction of light back-reflected from scattering components in the squeezing injection path to the IFO is achieved. Note that this isolation unit (consisting of one FR and 2 PBS's) is passed twice by the squeezed vacuum beam. We assume that at least one more isolation unit is needed in order to have sufficient optical isolation of the squeezing path. As a slightly conservative approach we will account optical losses for 3 isolation units (one for the injection, passed twice, and 2 for additional optical isolation), but in turn we will neglect additional small optical losses from required lambda-half wave plates and other transmitted optics in the injection path. If it turns out that 1 additional isolator is sufficient, we have a small spare loss budget.

The FR units used in the GEO 600 setup have a loss of 0.6 % per pass, a clear aperture of 2 cm diameter and are compatible with in-vacuum usage, such that we consider their design suitable as baseline design for LIGO3. We assume a loss of 0.5 % can be achieved. The PBS's currently in use in the GEO setup have a high loss of 1 % per pass, so here a large improvement is needed. An ultra-low loss PBS design with excellent separation of polarizations has been proposed and tested by Skeldon et.al. [57], with a loss as low as 200 ppm. Research is needed to see if this approach is suitable for sufficiently large aperture, but we take this as a basis to assume a loss of 0.05 % per PBS. Thus in total we account for $4 \times (0.5 \% + 2 \times 0.05 \%) \approx 2.4 \%$ loss for optical isolation and injection (squeezed vacuum passes in total 4 times through one of the 3 isolation units).

7.2.3 Mode matching

Experience at GEO 600 has shown that mode matching efficiencies of the squeezing (bright) beam to the OMC of 98-99 % are possible. Mode matching of the main IFO beam to the output mode cleaner (OMC) is more difficult, since more suspended optical components are involved, and typically the IFO dark port beam is composed of many different spatial modes. Further, the parameters for tuning the mode matching are much more restricted. Recently in GEO the main IFO mode-matching to the OMC was estimated to be 95-98 %, such that a mode matching of 99 % seems not completely out of reach. Probably some in-situ actuation on the mode matching parameters is needed in future. This could be done with remotely movable optics and/or thermally adjustable radii of curvature of optics. Similar arguments hold for the mode matching of the squeezed vacuum beam to the filter cavity, such that we assume $3 \times 1 \%$ loss for all involved cavity mode matchings.

7.2.4 OMC loss and quantum efficiency of detection photodiodes

Without accounting for a specific OMC design, we think that an overall loss of light power inside the OMC of no more than 0.5 % can be achieved. For the photodiode, it seems reasonable that with slightly more research, a quantum efficiency of 99.5 % can be reached. The photodiodes used in GEO 600 already have a quantum efficiency of 99 %. These units (produced by the Fraunhofer Institute in Berlin) have a diameter of 3 mm, and an AR-coating for an angle of incidence of 20 Degrees.

7.2.5 Losses due to phase noise and alignment signal split-off beams

Squeezing in GEO and LIGO has shown the importance of phase noise in the control loop that adjusts the squeezing ellipse orientation to match the required angle with respect to the interferometer output beam. An appropriate error signal with sufficient signal-to-noise ratio is required for this task. If the signal used for this control is shot-noise limited, a larger SNR can be obtained by detecting more light. If, however, detecting more light for this purpose means to split off more light power from the dark port beam (and thus decrease the detected light power) the overall losses would increase in a counter-productive manner. One way to detect more light without decreasing the light power in the main detection path, is to use the beam in reflection of the OMC. Here one measures the beat of the coherent control beam with the main IFO heterodyne modulation



sidebands. This control scheme already works in GEO. Further possibilities of generating a sufficiently good error signal have to be explored as well, as for example to investigate the limit to which the coherent control sidebands can be increased.

Another potential loss path is any split-off path at the IFO output where light is taken from the main beam for the purpose of auxiliary signal generation. A typical example is the generation of alignment signals for the main IFO. Depending on the requirements of the main IFO, a 'loss' of 1% or lower might be possible here. We leave this potential loss out of the budget here, but ways have to be found to generate alignment signals with as small as possible loss for the main beam. Perhaps the beam reflected at the OMC can also be explored for this.

7.2.6 Summary of squeezing losses

The optical losses according to the above statements summarize as follows:

- Generation of squeezing: 3%
- Optical isolation: 3 x 0.8%
- Mode matching to IFO and to OMC: 2 x 1%
- OMC loss and QE of PD: 2 x 0.5%
- Mode matching to filter cavity: 1%

Multiplying these loss factors yields 9% of loss, to which the frequency-dependent losses of the filter cavity have to be added.

7.3 Filter cavity for frequency-dependent squeezing

The broadband aLIGO configuration allows us to implement the optimal quantum-noise filter for the entire detection band using only one Fabry-Pérot cavity [58]. This is a major advantage compared to the general case where several filter cavities are required to achieve optimal filtering [59, 60]. The remaining question is if the filter cavity should be implemented as input or output filter. The input filter optimizes an externally generated squeezed field, whereas the output filter can fulfill the same function and in addition also optimize the readout quadrature. The reason why the output filter may not be the best choice is that its performance depends more critically on optical losses in the filter cavity than it does for the input filter.

We can understand this easily by first recalling that in the broadband configuration the radiation-pressure noise is simply ponderomotive anti-squeezing generated in the arm cavities. The squeezing factor is very large and so a small rotation of the squeezing ellipse by an output filter has a big effect on quantum noise. A lossless output filter could in principle eliminate all radiation-pressure noise, but a small cavity loss can completely forfeit this advantage over the input filter or even cause additional noise as we will see in the following. Figure 12 shows the quantum noise and signal strength with output filter. Loss in the filter cavity causes mixing of the squeezed output field with coherent vacuum, which causes quantum noise to increase near the frequency that corresponds to half the bandwidth of the filter cavity. In addition, filter loss causes a deviation from optimal filtering such that the ponderomotively squeezed field is detected in a weakly squeezed, or anti-squeezed quadrature depending on the loss value. Now this can still mean that radiation-pressure noise is partially cancelled, but it turns out that the sensitivity of the detector towards GW signal is smaller than in the input filter case since the output filter also causes a partial transfer of GW signal from the detected quadrature into the undetected one. This effect is shown in the right plot of figure 12. For a 100 m filter cavity, the output filter performs better if the round-trip loss in the cavity is smaller than 4 ppm! These very small loss values are beyond reach at the moment. The consequence is that the filter should be implemented as *input filter*. In figure 13 another comparison is shown between various detector configurations. Except for filter-cavity loss, all curves are drawn for a lossless interferometer to simplify the comparison between the two filter types. The plots show that the output filter

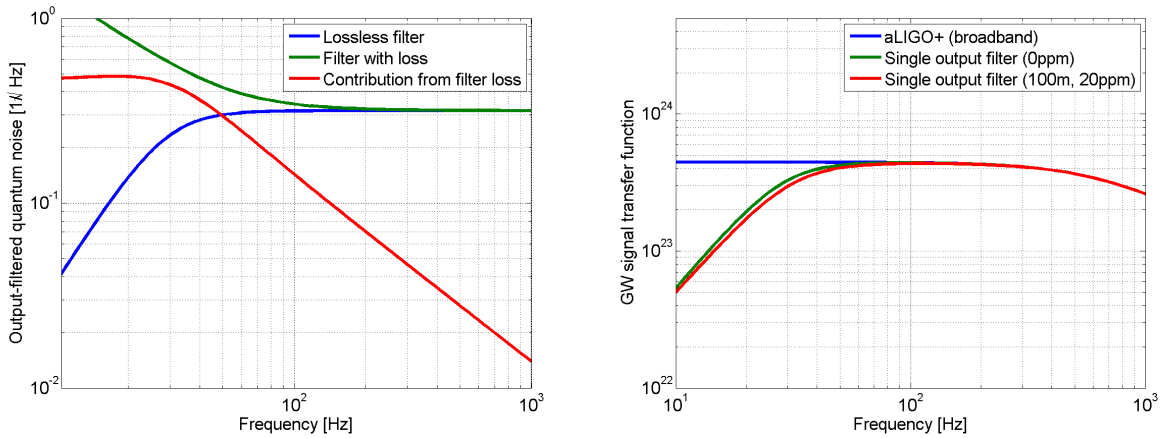


Figure 12: The plot to the left shows the quantum-noise spectra for a lossless 100 m output filter and a filter with 20 ppm loss. For the case of the filter with loss, the contribution from the coherent vacuum is plotted explicitly. The additional noise comes from improper filtering and therefore residual ponderomotive anti-squeezing. Even though quantum noise is still reduced with respect to the unfiltered case, the sensitivity to GWs is smaller as is explained by the plot to the right. The GW signal is partially transferred by the output filter into the undetected quadrature causing an overall decrease of GW sensitivity for the output filter with loss.

wins in noise reduction, but that the GW sensitivity is better with input filter assuming 20 ppm round-trip loss. As the desired round-trip loss for the input filter will be of order 20 ppm depending on the final choice of cavity

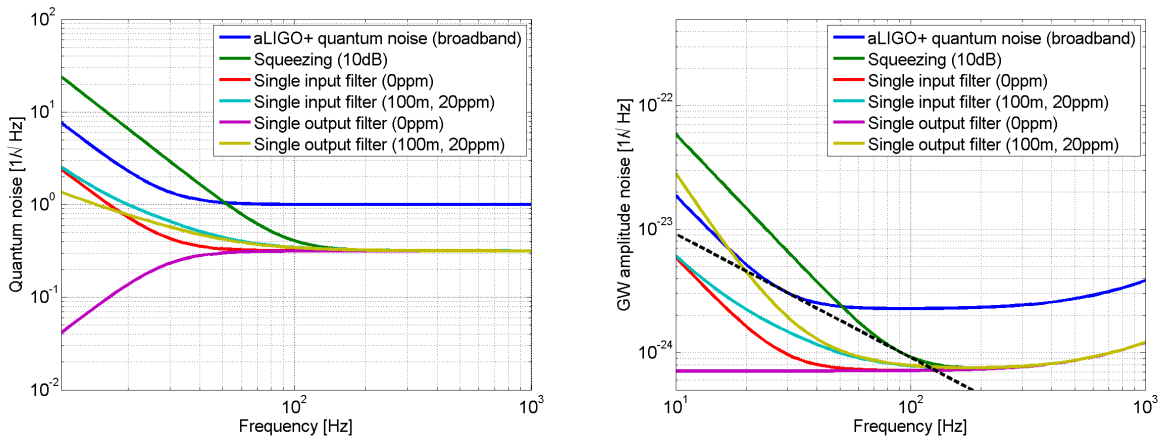


Figure 13: The plot to the left shows quantum-noise spectra for various configurations. Only the curve labelled as broadband is without external squeezing, all other curves are drawn for 10 dB external squeezing. The output filter yields highest noise reduction. However, the sensitivity curves reveal that the output filter with loss performs worse in terms of signal-to-noise ratio than the input filter, which was explained in the previous figure.

length, it is evident that the foremost challenge of implementing filter cavities is to reduce optical loss. The results of past loss measurements are summarized in table 4. In addition to the cited values, round-trip loss in the km-scale arm cavities of the second-generation GW detectors is expected to be of the order of 100 ppm. We see that loss can be very small in short cavities with small beam size. The dominant loss mechanism is optical scattering. Usually, scattering is further divided into surface-roughness and point-defect scattering. Scatter loss decreases substantially with decreasing beam size. Starting from 10 cm scale beams the main effect of smaller beam size is that surface-roughness becomes less significant. Further decreasing the beam size, one eventually



Length [m]	Loss per mirror [ppm]	Year
10	60	1984 [61]
0.004	1.1	1992 [62]
0.202	1.5	1996 [63]
0.202	1.6	1998 [64]
20	30	1999 [?]

Table 4: Summary of previous cavity loss measurements.

hits a limit when point-defect scattering becomes dominant, which is independent of beam size. This however is only true as long as the beam size is larger than the mean distance between point defects. The lowest loss values documented in the table are a result of steering a very small beam into regions of the mirror surface that are free of point defects. Since beam size on mirrors of a 100 m cavity would be sub-cm, it is conceivable that point-defect scattering will be dominant. The only way to make robust loss predictions is to measure loss in prototype cavities and compare with results from numerical simulations.

Since at this point no robust loss predictions can be made for the filter cavity, we will present results for various cavity lengths assuming a fixed round-trip loss of 30 ppm. As discussed above, round-trip loss in reality depends on cavity length. The purpose here is to present a simplified parameter study. Figure 14 shows the sensitivity gain as a function of cavity length with fixed loss. A 50 m filter cavity with 30 ppm round-trip loss does not seem attractive, but large increase in NS/NS inspiral range can be achieved if the same loss can be realized in a 300 m filter. Some of the results are again summarized in table 5.

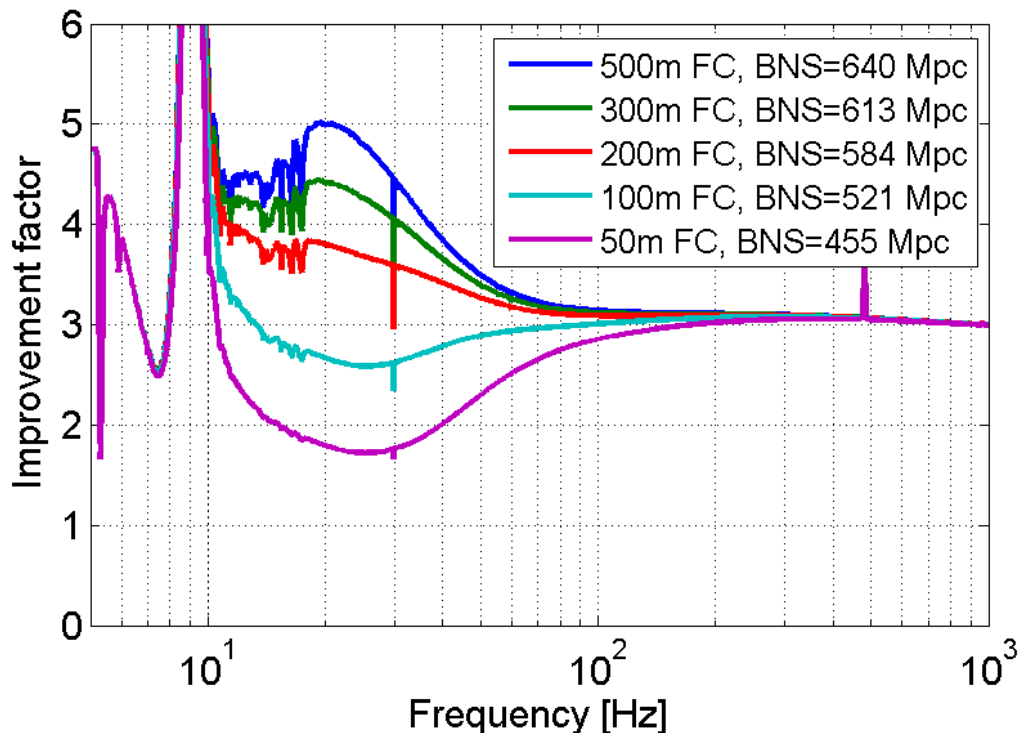


Figure 14: Overall sensitivity improvement of the strawman red design over the Advanced LIGO baseline sensitivity for the various input-filter cavity lengths. The improvement factor is based on the full noise spectrum of the strawman design. The following assumptions have been made regarding the squeezing: 20dB initial squeezing, 9% losses (mode matching, FI, photodiodes etc) and a round-trip loss of 30 ppm inside the filter cavity.



Filter cavity length [m]	500	300	200	100	50
Input mirror power transmittance [ppm]	704	422	281	141	70
Binary neutron star inspiral range [MPc]	640	613	584	521	455

Table 5: Filter-cavity parameters and performance for various cavity lengths. Assumed is a length independent round-trip loss of 30 ppm. All configurations have a common optimal cavity detuning of -16.7 Hz.

One potential risk associated with input filters is that it could increase low-frequency quantum noise by wrongly orienting the squeezing ellipse. Our results indicate that sensitivity gain can be achieved even if the round-trip loss is wrongly predicted by factors of two and higher, but this does not take into account that the input field will have larger anti-squeezing than squeezing due to optical loss. We suggest to carry out careful analyses of the filter performance with respect to uncertainties in round-trip loss. Also it is conceivable that input transmittance of the filter cavity will deviate significantly from its optimal value.

7.4 Required Hardware

Here should go a short list of hardware required for the frequency dependent squeezing. Just a quick explanation of the items shown in the costing.

7.5 Alternative Solutions

7.5.1 Speedmeter

It has been suggested from theoretical analysis that an interferometer measuring velocity or momentum of the test masses instead of its position would not be susceptible to the SQL [65]. The most promising approach for such a speedmeter device is a velocity sensitive Sagnac interferometer, which would allow to significantly surpass the SQL (sub-SQL measurement).

Figure 16 shows the comparison of the advanced LIGO quantum noise and a Sagnac speedmeter of similar length and optical power. As one can see the speedmeter gives for a roughly similar bandwidth, a strongly increased low frequency sensitivity, because the back action noise is suppressed. While the quantum noise of Advanced LIGO follows a $1/f^2$ slope at low frequencies, the quantum noise of the speedmeter follows a $1/f$ -slope which originates from the optical response of the Sagnac interferometer.

However, currently there is very little experimental experience with speedmeter configuration and it would be important to carry out further R&D efforts to shed more light on their experimental realisation and the associated technical challenges.

Within this document we restrict our effort on speedmeter configurations a sensitivity analysis of a Sagnac speedmeter with arm cavities and frequency dependent squeezing using one filter cavity. A detailed description of the calculations can be found in Appendix A.

The parameters of the here considered speedmeter configurations with a short (100 m) and a long (4 km) filter cavity are given in table 6 and the corresponding noise budget is shown in Figure 15. Please note the very low quantum noise at low frequencies which was actually achieved with mirrors of only 40 kg. However, as the overall sensitivity is not so much different from the Strawman Red sensitivity shown in Figure 2, because at low frequencies the quantum noise is masked by other noise sources.

7.5.2 Local Readout schemes

There are two possible variants proposed as local readout schemes, both of which utilise the optical spring effect to enhance sensitivity. In the first option, ‘Local Readout’ [54], a conventional aLIGO dual recycled Fabry Perot



Parameter	Description	Value (4-km filter cavity)	Value (100-m filter cavity)
M	Mirror mass	40 kg	40 kg
L	Arms length	3995 m	3995 km
λ_0	Laser wavelength	1.064 μm	1.064 μm
P_c	Power in arms	2×750 kW	2×750 kW
η	quantum efficiency of PD	95%	95%
ϵ_{arm}	round-trip loss in arms	40 ppm	40 ppm
ϵ_{FC}	round-trip loss in FC	40 ppm	40 ppm
ζ	optimal homodyne angle	6.43 degrees	15 degrees
e^{2r}	squeezing factor	10 dB	10 dB
ψ_0	constant squeezing phase shift	6.46 degrees	15.5 degrees
T_{ITM}	ITM power transmissivity	0.052	0.06
$T_{\text{SRM}} = 1 - \rho_{\text{SR}}^2$	SRM power transmissivity	0.89	0.9
ϕ_{SRC}	SR cavity detune phase	90	73.7 degrees
T_f	FC input mirrot power transmissivity	0.017	0.023
L_f	FC length	3.995 m	100 m
$\gamma_f = \frac{cT_f}{4L_f}$	FC half-bandwidth	$2\pi \times 49 \text{ sec}^{-1}$	$2\pi \times 540 \text{ sec}^{-1}$
δ_f	FC detuning	$2\pi \times 32 \text{ sec}^{-1}$	$2\pi \times 255 \text{ sec}^{-1}$

Table 6: Optimal parameter for the Sagnac speedmeter obtained by numerical optimisation.

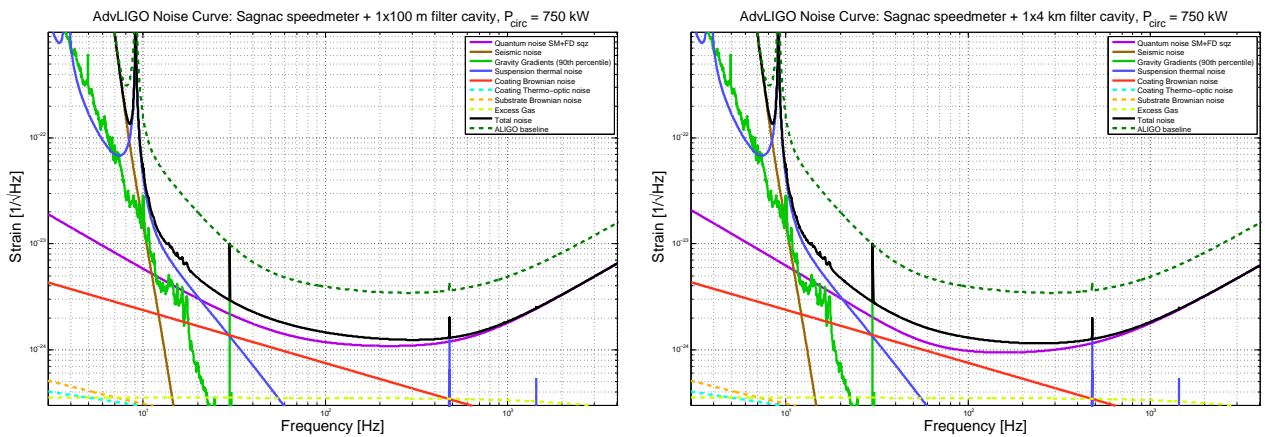


Figure 15: Sensitivity curves for Sagnac speedmeter with ventional FPM optimal parameters. *Left panel:* Short 100-m input filter cavities; *Right panel:* Long 4-km input filter cavities.



configuration is utilised and arranged for optical rigidity such that, below the optomechanical resonance, the arm cavity inner test masses are rigidly coupled to the end test masses. In effect, this is a standard optical spring in each arm and the inner test masses can be considered to be actuated by a passing gravitational wave. A second laser is then injected into the interferometer at a frequency offset from the first such that it does not resonate in the arm cavities. This laser locally reads out the motion of the inner test masses and potentially improves the low frequency performance of the instrument.

One potential issue with the above method, is that optical springs have intrinsic instabilities associated with them. While it is possible to correct for this via feedback techniques, a more elegant second method was devised - the 'Dual Carrier' scheme [66]. In essence it is identical to the Local Readout method, except the second laser is also resonant in the arm cavities. By carefully setting the laser amplitudes and frequencies, it is possible to create a spring with one laser and an anti-spring with the other such that the combined system is stable. Again, the advantage of this scheme is primarily low frequency sensitivity over more conventional topologies.



8 Acknowledgements

The authors would like to thank Ernst-Bernhard Kley and Stefanie Kroker for useful discussions on the fabrication process of waveguide coatings and Daniel Friedrich for the noise calculations of wave guide mirrors. We are also grateful to Daniel Sigg and Christan Graef for useful comments on aspects of the injection of squeezed light and the Khalili cavities, respectively. Rodica Martin, John Worden, Mike Zucker and Fabrice Matichard have given input to the cost evaluations of the presented design. We would also like to thank Henning Vahlbruch for useful discussions on squeezing sources.

A Sagnac-Speedmeter with frequency dependent squeezing

Speedmeter's well known ability to outperform a conventional Fabry-Pérot-Michelson (FPM) interferometer in terms of quantum noise at low frequencies (see Figure 16) makes it an interesting alternative to the conventional AdvLIGO strawman design.

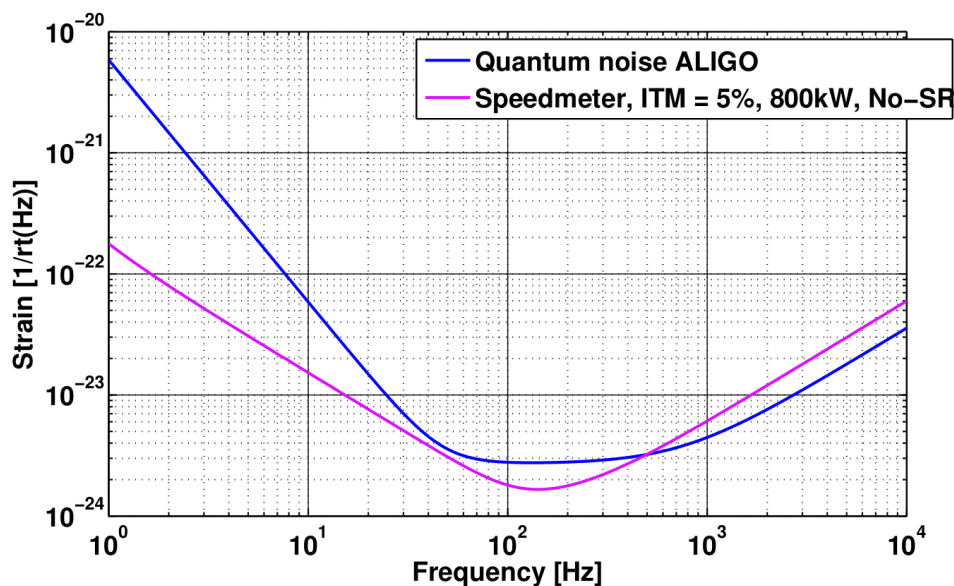


Figure 16: Quantum noise comparison of Advanced LIGO and a Sagnac speedmeter without signal recycling, but otherwise similar optical parameters (losses, intracavity power etc). While at high frequencies the Michelson interferometer provides a better sensitivity, the speedmeter gives significantly improved low-frequency sensitivity, due to the evasion of back-action noise.

Radiation pressure noise suppression in speedmeters. Low-frequency part of quantum noise of any interferometric GW-detector is known to be dominated by radiation pressure fluctuations. Speedmeter's improved performance at these frequencies follows from the special way it responds to the mechanical motion of the test masses. To see how it works consider the speedmeter based on a zero-area Sagnac interferometer first proposed by Y. Chen [67] and drawn in Fig. 17.

For simplicity, we consider first a case with tuned signal recycling cavity (in speedmeter it corresponds to $\phi_{\text{SRC}} = \pi/2$) where all the main features of the speedmeter can be seen clearly. For more general analysis of detuned recycled speedmeter one can resort to comprehensive study by H. Müller-Ebhardt [68].

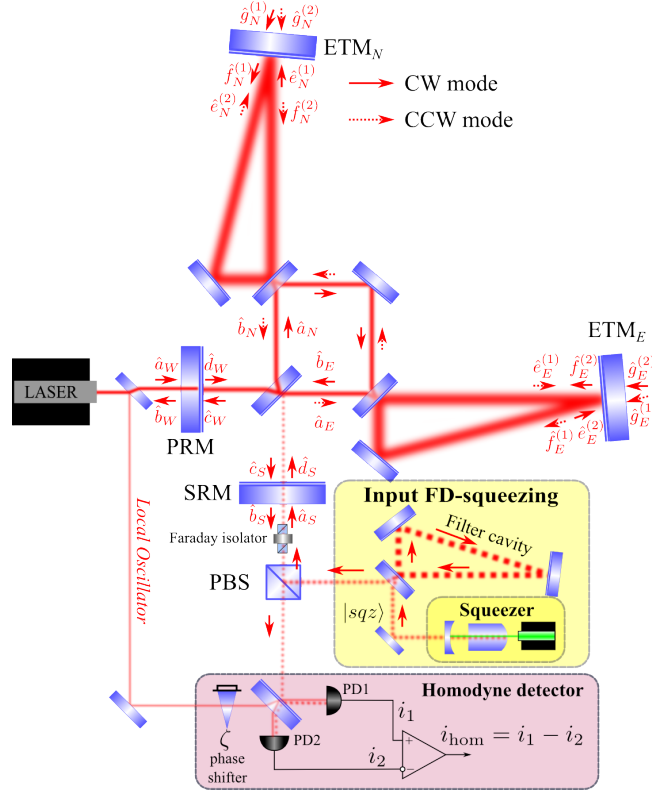


Figure 17: Scheme of signal- and power-recycled Sagnac speedometer with frequency-dependent input squeezing provided by a single filter cavity.

Employing the two-photon formalism of Caves and Schumaker [69, 70], the speedometer output field (denoted by \hat{b}_S in Fig. 17) can be expressed in a very clear form introduced in [71] in terms of input field \hat{a}_S as:

$$\begin{bmatrix} \hat{b}_1 \\ \hat{b}_2 \end{bmatrix} = -e^{2i\beta} \begin{bmatrix} 1 & 0 \\ -\mathcal{K}_{SM} & 1 \end{bmatrix} \begin{bmatrix} \hat{a}_1 \\ \hat{a}_2 \end{bmatrix} + \begin{bmatrix} 0 \\ \sqrt{2\mathcal{K}_{SM}} \end{bmatrix} e^{i\beta} \frac{h}{h_{SQL}}. \quad (6)$$

Here $\hat{a}_{1(2)}$ and $\hat{b}_{1(2)}$ stand for cosine (sine) quadratures of the input (\hat{a}_S) and output (\hat{b}_S) quantum fields at the signal port of the speedometer, $\beta = \arctan(\Omega F / \gamma) + \arctan(\Omega / (F \gamma))$ is the irrelevant frequency-dependent phase shift (it does not appear in the final expressions for quantum noise spectral densities),

$$h_{SQL} = \sqrt{\frac{8\hbar}{M\Omega^2 L^2}} \quad (7)$$

is the amplitude (single-sided) spectral density of the standard quantum limit (SQL) written in terms of GW strain amplitude h for an interferometer with mirror masses M and arm-lengths L . The expressions (6) are very similar to those for an ordinary Fabry-Pérot-Michelson (FPM) interferometer [cf. Eq. (16) of [71]] save to the shape of the optomechanical coupling constant $\mathcal{K}_{SM}(\Omega)$:

$$\mathcal{K}_{SM} = \frac{4\Theta\gamma F}{\Omega^4 + \gamma^2\Omega^2(F^2 + F^{-2}) + \gamma^4}, \quad \text{with } \gamma = \frac{c(T_{ITM} + T_{ETM})}{4L}, \quad \text{and } F = \frac{1 - \sqrt{\rho_{SR}}}{1 + \sqrt{\rho_{SR}}} \quad (8)$$

where T_{ITM} (T_{ETM}) is the power transmissivity of the input (end) mirror of the arm cavity and ρ_{SR} is the *amplitude* reflectivity of the signal-recycling mirror (SRM), while for Fabry-Pérot-Michelson with the same optical parameters it takes the following form:

$$\mathcal{K}_{FPM} = \frac{2\Theta\gamma}{\Omega^2(\gamma^2 + \Omega^2)}. \quad (9)$$



Here $\Theta = 4\omega_0 P_c / (McL)$ is the constant having the dimension of frequency cubed and depends on optical power P_c , circulating in the interferometer⁶, and ω_0 is a pump laser frequency. The frequency $\Omega_* = \sqrt[3]{\Theta}$ has its own special meaning: it is the central frequency of the region where the interferometer has its best sensitivity.

The optomechanical coupling constant \mathcal{K} reflects, on the one hand, how the interferometer transforms the GW signal h to the modulation of the output light (transfer function is $\propto \sqrt{2\mathcal{K}}/h_{\text{SQL}}$)⁷ and, on the other hand, it describes the back-action (radiation-pressure) noise contribution to the readout light phase quadrature \hat{b}_2 (that bears information about GW signal) by a means of an additional term $-\mathcal{K}\hat{a}_1$. It is this term that makes the light, passing through the interferometer, to suffer (frequency-dependent) ponderomotive squeezing with squeezing factor $r_{\text{pond}}(\Omega)$ and squeezing angle $\lambda_{\text{pond}}(\Omega)$ hinging on \mathcal{K} :

$$e^{r_{\text{pond}}} = \sqrt{1 + (K/2)^2} + K/2, \quad \lambda_{\text{pond}} = \frac{1}{2} \arccot \frac{K}{2}, \quad (10)$$

as drawn in panels (b) and (c) of Fig. 18. The evident fact that at low frequencies the optomechanical coupling

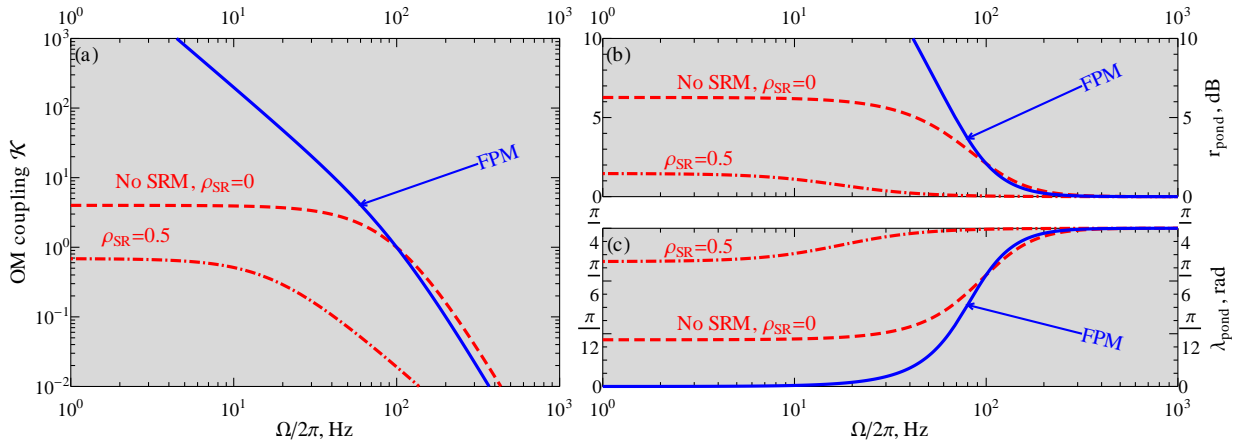


Figure 18: Ponderomotive squeezing in interferometers. (a) Optomechanical coupling constant of tuned FPM-interferometer (blue solid curve), tuned Sagnac speedmeter w/o signal recycling (red dashed curve) and with signal recycling mirror of moderate reflectivity $\rho_{\text{SR}}^2 = 0.25$ (red dash-dotted curve); (b) ponderomotive squeezing factor $r_{\text{pond}}(\Omega)$ for the same interferometers; (c) frequency dependence of the ponderomotive squeezing angle $\lambda_{\text{pond}}(\Omega)$ for the same interferometers. We assume $\gamma/2\pi = 100$ Hz and $\Theta = (2\pi 100 \text{ Hz})^3$ which corresponds to $P_c \sim 2 \times 840$ kW of optical circulating power.

constant (as well as ponderomotive squeezing factor r_{pond}) of the FPM tends to infinity, as drawn in panel (a) of Fig. 18, while that of the speedmeter just reaches the constant value:

$$\mathcal{K}_{\text{FPM}}(\Omega \rightarrow 0) \rightarrow \infty, \quad \mathcal{K}_{\text{SM}}(\Omega \rightarrow 0) = \frac{4\Theta F}{\gamma^3} = \text{const}. \quad (11)$$

is a vivid manifestation of the reduced back-action noise of the latter, which is the first big argument in favor of the speedmeter over the FPM.

Input squeezing. Let us consider now a quantum noise spectral density of the lossless tuned interferometer with input squeezing, characterised by squeezing factor r (10 dB squeezing corresponds to $r \simeq 1.152$) and squeezing angle λ (phase squeezing corresponds to $\lambda = 0$), and homodyne readout with homodyne angle ζ (GW

⁶Note that for given power at the beamsplitter, P_{BS} , the power circulating in the arms of the Sagnac speedmeter is twice of that in the FPM-interferometer: $P_c^{\text{SM}} = 2P_c^{\text{FPM}}$!

⁷Note also that in tuned case signal recycling is not of much use and optimal OM coupling is obtained when $F \rightarrow 1$ that is achieved without SRM: $\rho_{\text{SR}} = 0$.



signal is in phase quadrature defined as $\zeta = \pi/2$):

$$S^h = \frac{h_{\text{SQL}}^2}{2} \left\{ \frac{e^{2r}(\sin \lambda + \cos \lambda [\mathcal{K} - \cot \zeta])^2 + e^{-2r}(\cos \lambda - \sin \lambda [\mathcal{K} - \cot \zeta])^2}{\mathcal{K}} \right\}. \quad (12)$$

If one assumes phase squeezing, it is evident that radiation pressure noise can be eliminated from the readout provided that

$$\zeta = \text{arccot} \mathcal{K}. \quad (13)$$

However, for \mathcal{K} is frequency dependent, it is not clear how to provide the required frequency dependence of ζ right away. In the case of FPM, the most straightforward solution is the use of additional output filter cavities as proposed by Kimble *et al.* [71], that involves additional and rather high expenses, to say nothing about the optical loss issue that makes output filters almost useless at low frequencies (see, *e.g.*, the review [72]). Speedmeter, however, allows to reach the same effect, without any additional filters just due to the fact that $\mathcal{K}_{\text{SM}}(\Omega) \rightarrow \text{const}$ at low frequencies, where back-action noise resides, and thus it is sufficient to set ζ to a constant value:

$$\zeta_{\text{SM}} = \text{arccot} \mathcal{K}_{\text{SM}}(0) = \text{arccot} \frac{4\Theta F}{\gamma^3}. \quad (14)$$

Here we get the second serious advantage of the speedmeter. However, there is a drawback concerning this solution: at high frequencies the performance of such a speedmeter is somewhat inferior to that of the FPM, as the uncompensated back-action at the frequencies $\Omega \gg \gamma$ is amplified by the anti-squeezing factor e^{2r} and dominates that region:

$$S_{\text{SM, b.a.}}^h(\Omega \gg \gamma) \simeq \frac{h_{\text{SQL}}^2}{2} \frac{4\Theta \Omega^4 e^{2r}}{\gamma^7} \gg S_{\text{SM, shot noise}}^h(\Omega \gg \gamma) = \frac{h_{\text{SQL}}^2}{2} \frac{\Omega^4 e^{-2r}}{4\Theta \gamma}. \quad (15)$$

Frequency-dependent input squeezing. Can we do anything about this drawback? Sure, if one employs input squeezing with frequency-dependent angle $\lambda(\Omega)$, such that (cf. Eq. (16) of [73]):

$$\cot \zeta - \tan \lambda(\Omega) = \mathcal{K}(\Omega). \quad (16)$$

If by some means the above frequency dependence is reached, the effect would be the reduction of quantum noise in all frequencies by a squeezing factor e^r (in amplitude) yielding the following transformation of Eq. (12):

$$S^h = \frac{h_{\text{SQL}}^2 e^{-2r}}{2} \left\{ \frac{1 + [\mathcal{K} - \cot \zeta]^2}{\mathcal{K}} \right\}. \quad (17)$$

The corresponding sensitivity curves can be found in panel (a) of Fig. 19

An optimal frequency dependence of the squeezing angle can be achieved if one lets the squeezed light from the squeezer to reflect off the phase-rotating filter cavity that, in lossless limit, provides frequency-dependent phase rotation of the reflected light field given by the following formula:

$$\lambda_f(\Omega) = \arctan \frac{2\gamma_f \delta_f}{\gamma_f^2 - \delta_f^2 + \Omega^2}, \quad (18)$$

where $\gamma_f = cT_i/(4L_f)$ and δ_f are the filter cavity half-bandwidth and detuning, respectively, and T_i stands for a filter input mirror power transmissivity while L_f is its length. It should be noted that additional constant phase shift ψ_0 should be added to the initial field to approximate the optimal dependence of Eq. (16), that is shown in Fig. 19 for both, the FPM interferometer and the speedmeter.

Optical losses. Optical losses is the main problem and the main limiting factor of any quantum-noise-limited GW interferometer. Speedmeter is not an exception, unfortunately. However, it is much more robust to losses than the advanced interferometers based on FPM as was shown in [72, 74, 75]. Purdue and Chen carried out an

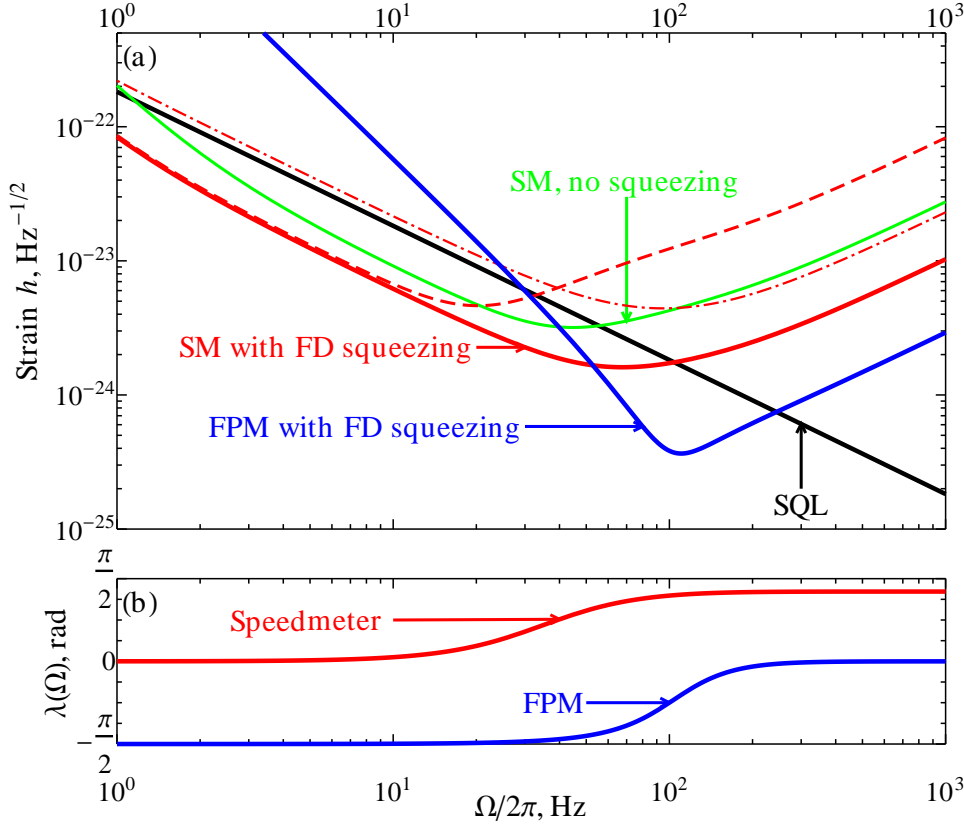


Figure 19: Sensitivity of speedmeter with input squeezing. (a) Sensitivity curves for speedmeter w/o squeezing (green solid curve), with phase ($\Lambda = 0$) squeezing (red dashed curve), with amplitude ($\Lambda = \pi/2$) squeezing (red dash-dotted curve), with optimal frequency dependent squeezing (red solid curve) and sensitivity curve for FPM with optimal FD squeezing (blue solid curve). (b) Optimal squeezing angle for speedmeter (red solid curve) and FPM interferometer. All curves are plotted in assumption of 95% quantum efficiency of readout photodetectors and round-trip loss in the arm cavities $\epsilon_{\text{arm}} = 100$ ppm. We assume also $\gamma/2\pi = 100$ Hz and $\Theta = (2\pi 100 \text{ Hz})^3$ which corresponds to $P_c \sim 2 \times 840$ kW of optical circulating power.

extensive analysis of the influence of optical loss that arise in different elements of the speedmeter interferometer (see Sec. V of [74])⁸. It was shown that the major contribution to quantum noise is due to losses in the readout train of the interferometer. Moreover, without sacrificing the generality, these losses can be all reduced to the finite quantum efficiency η of the photodetectors that allows to rewrite the readout photocurrent of the lossy interferometer as a sum of that of the lossless one and an additional vacuum field \hat{n} modelling the losses in the detector:

$$\hat{b}_\zeta^{\text{loss}} = \sqrt{\eta}(\hat{b}_1 \cos \zeta + \hat{b}_2 \sin \zeta) + \sqrt{1 - \eta} \hat{n}. \quad (19)$$

For in speedmeter a carrier light passes through both the arm cavities sequentially, there is another important loss source that limits its sensitivity at low frequencies. It arises due to losses in the arm cavities that can be modeled by finite transmissivity of the ETMs that we will characterise by the round trip loss coefficient ϵ_{arm} . The vacuum fields that enter the arm cavities through the ETMs (\hat{g} -fields in Fig. 17) couple to the carrier fields and generate an additional back action which has the same frequency dependence as that of the FPM interferometer, for these vacuum fields do not travel through both arm cavities contrary to the field that enters

⁸Though authors considered a different scheme of the speedmeter that uses an additional sloshing cavity coupled to a recycled FPM interferometer, the obtained results are fully applicable with very minor and insignificant variations to Sagnac speedmeter as well.



the interferometer through the signal port. As shown in [72] the spectral density of the lossy speedmeter with both these loss factors taken into account reads:

$$S_{\text{SM}}^{h, \text{loss}} = \frac{h_{\text{SQL}}^2}{2} \left\{ \frac{e^{2r}(\sin \lambda + \cos \lambda [\mathcal{K}_{\text{SM}} - \cot \zeta])^2 + e^{-2r}(\cos \lambda - \sin \lambda [\mathcal{K}_{\text{SM}} - \cot \zeta])^2}{\mathcal{K}_{\text{SM}}} + \frac{\xi_{\text{loss}}^2}{\mathcal{K}_{\text{SM}} \sin^2 \zeta} + \xi_{\text{arm}}^2 \mathcal{K}_{\text{FPM}} \right\}, \quad (20)$$

where $\xi_{\text{loss}} = \sqrt{(1-\eta)/\eta}$ is the loss factor due to inefficiency of detection at the readout and $\xi_{\text{arm}} = \sqrt{\epsilon_{\text{arm}}/(1-\epsilon_{\text{arm}})} \simeq \sqrt{\epsilon_{\text{arm}}}$ is the loss factor due to optical losses in the arm cavities. The effect of optical loss in the arm cavities can be clearly seen in panel (a) of Fig. 19 where sensitivity curves start to go up at very low frequencies. The readout loss is the most notorious one and makes the whole sensitivity curve to raise closer to the level of SQL. As shown in [72] there is a limit by how far any SQL-beating scheme can dive below the SQL at the given level of optical loss ξ_{loss} and with using of input squeezing with squeezing factor e^{2r} :

$$\frac{h}{h_{\text{SQL}}} \geq \xi_{\text{loss}} \sqrt[4]{\frac{e^{-2r} + \xi_{\text{loss}}^2}{1 + \xi_{\text{loss}}^2 e^{-2r}}}. \quad (21)$$

At low frequencies speedmeter sensitivity curve follows this limit.

In the configuration with input filter cavities the round-trip absorption in the latter also contributes significantly to the quantum noise, for it effectively makes squeezed light to mix up with the vacuum fields entering the cavity through the lossy mirrors. This effects in raising of the quantum noise curve a little bit more at low frequencies (see plots in Fig. 15).

Optimisation of Sagnac speedmeter. In order to find the optimal configuration of the Sagnac speedmeter with input filter cavities drawn in Fig. 17 for given technical noise budget a numerical optimisation is required. We carried it out setting the following cost function proposed by Rana Adhikari for broadband numerical optimisation of GW detectors:

$$C(\vec{p}) = \int_{f_{\text{min}}}^{f_{\text{max}}} \log_{10} [S_{\text{quant}}^h(f; \vec{p}) + S_{\text{tech}}^h(f)] d \log_{10} f, \quad (22)$$

where $f = \Omega/2\pi$ is integration frequency, $f_{\text{max}} = 4040$ Hz is upper bound frequency, $f_{\text{min}} = 1$ Hz is lower bound frequency, $S_{\text{quant}}^h(f; \vec{p})$ stands for quantum noise spectral density that depends on the set of optical parameters given by a vector \vec{p} to be optimised over, and $S_{\text{tech}}^h(f)$ is the sum spectral density of the technical noise sources.

We optimized the cost function $C(\vec{p})$ over $\vec{p} = \{T_{\text{ITM}}, T_{\text{SRM}}, \phi_{\text{SRC}}, \zeta, \psi_0, \gamma_f, \delta_f\}^T$ using standard Nelder-Mead simplex method realised in program written in C using standard GNU Scientific Library (GSL) function `gsl_multimin_fminimizer_nmsimplex2` for multidimensional minimisation. The results of this optimisation as well as explanation of all parameters are given in Table 6 and the corresponding sensitivity curves are plotted in Fig. 15 for two cases of short (left panel) and long (right panel) filter cavities.

Some concluding remarks. To summarise we can derive the following advantages of the speedmeter as an alternative to conventional interferometers:

1. Speedmeters have way better performance than the FPM at low frequencies due to depressed back-action noise that remains constant in this region contrary to that of the FPMI;
2. Due to the same feature it allows for constant homodyne readout phase that appears to be optimal at low frequencies;
3. They are much less susceptible to optical losses than FPMI;



4. The requirements to signal-recycling mirror might be less stringent than for the FPM, for optimal configuration requires almost transparent SRM;
5. Decent broadband sensitivity can be obtained with tuned recycling cavity (note that for speedmeter it corresponds to $\phi_{\text{SRC}} = \pi/2$);
6. The requirements for frequency-dependent squeezing setup are also not too tough, for relatively short single filter cavity with reasonable bandwidth suffices for decent sensitivity, though the longer it would be, the better in terms of optical loss (it scales as (round-trip power loss)/(FC length)).

However, speedmeters have some soft spots to which one might concern:

1. lower than for FPM interferometers sub-SQL region (for the same circulating power), *e.g.*, the band of frequencies where speedmeter overcomes the SQL, and thus less impressive performance at higher frequencies;
2. need for either ring arm cavities or polarisation optics to provide the speedmeter specific optical path inside the main interferometer;
3. back-scattering loss in the ring cavities or polarisation mismatch that may lead to unwanted Michelson-like signal fraction in the readout quadrature.



References

- [1] J. Abadie, T. L. S. Collaboration, and the Virgo Collaboration, “Predictions for the rates of compact binary coalescences observable by ground-based gravitational-wave detectors,” *Classical and Quantum Gravity*, vol. 27, no. 17, p. 173001, 2010.
- [2] N. Robertson et al., “Advanced LIGO Suspension System Conceptual Design,” *LIGO T010103*, 2006.
- [3] E. Eliffe et al., “Hydroxide-catalysis bonding for stable optical systems for space,” *Classical and Quantum Gravity*, vol. 22, pp. S257–S267, 2005.
- [4] A. Cumming et al., “Design and development of the advanced LIGO monolithic fused silica suspension,” *Classical and Quantum Gravity*, submitted 2011.
- [5] A. Heptonstall et al., “CO₂ laser production of fused silica fibers for use in interferometric gravitational wave detector mirror suspensions,” *Review of Scientific Instruments*, vol. 82, p. 011301, 2011.
- [6] L. Cuningham et al., “Re-evaluation of the mechanical loss factor of hydroxide-catalysis bonds and its significance for the next generation of gravitational wave detectors,” *Physics Letters A*, vol. 374, pp. 3993–3998, 2010.
- [7] A. Heptonstall et al., “Investigation of mechanical dissipation in CO₂ laser-drawn fused silica fibres and welds,” *Classical and Quantum Gravity*, vol. 27, p. 035013, 2010.
- [8] S. Penn et al., “Frequency and surface dependence of the mechanical loss in fused silica,” *Physics Letters A*, vol. 352, pp. 3–6, 2006.
- [9] A. Gretarrson and H. G.M., “Frequency and surface dependence of the mechanical loss in fused silica,” *Review of Scientific Instruments*, vol. 70, pp. 4081–4087, 1999.
- [10] G. Cagnoli and P. Willems, “Effects of nonlinear thermoelastic damping in highly stressed fibres,” *Physical Review B*, vol. 65, p. 174111, 2002.
- [11] A. Cumming et al., “Finite element modelling of the mechanical loss of silica suspension fibres for advanced gravitational wave detectors,” *Classical and Quantum Gravity*, vol. 26, p. 215012, 2009.
- [12] Y. Young and R. Budnas, *Roark’s formulas for stress and strain*. McGraw Hill, 2002.
- [13] V. Mitrofanov and TokmakovK.V., “Effect of heating on dissipation of mechanical energy in fused silica fibers,” *Physics Letters A*, vol. 308, pp. 212–218, 2003.
- [14] G. Harry, “Q’s of LASTI Violin Modes,” *LIGO T1000468*, 2010.
- [15] K. S. Thorne and C. J. Winstein, “Human gravity-gradient noise in interferometric gravitational-wave detectors,” *Physical Review D*, vol. 60, p. 082001, Oct. 1999.
- [16] T. Creighton, “Tumbleweeds and airborne gravitational noise sources for LIGO,” *Classical and Quantum Gravity*, vol. 25, p. 125011, June 2008.
- [17] S. A. Hughes and K. S. Thorne, “Seismic gravity-gradient noise in interferometric gravitational-wave detectors,” *Physical Review D*, vol. 58, p. 122002, Dec. 1998.
- [18] J. Harms, R. Desalvo, S. Dorsher, and V. Mandic, “Simulation of underground gravity gradients from stochastic seismic fields,” *Physical Review D*, vol. 80, p. 122001, Dec. 2009.
- [19] S. Waldman and P. Fritschel, “Reference seismic data for LLO,” *Tech. Report*, vol. LIGO-T0900312, 2009.
- [20] J. Driggers and J. Harms, “Results of phase 1 newtonian noise measurements at the ligo sites, february-march 2011,” *LIGO DCC*, vol. T1100237, 2011.
- [21] B. Baykant Alagoz and S. Alagoz, “Seismic Crystals And Earthquake Shield Application,” *ArXiv e-prints*, Feb. 2009.
- [22] J. Driggers, “Seismic scattering at the ligo sites,” *GWADW 2011 Elba talk*, 2011.



-
- [23] J. Driggers, M. Evans, K. Pepper, and R. Adhikari, “Active noise cancellation in a suspended interferometer,” *ArXiv*, vol. arXiv:1112.2224v1, 2011.
- [24] J. Harms, “Newtonian noise research at the aligo sites,” 2011.
- [25] J. Harms, R. DeSalvo, S. Dorsher, and V. Mandic, “Gravity-Gradient Subtraction in 3rd Generation Underground Gravitational-Wave Detectors in Homogeneous Media,” *ArXiv e-prints*, Oct. 2009.
- [26] J. Harms and B. O’Reilly, “Velocity and Attenuation Characterization of the LIGO Site near Livingston, Louisiana,” *The Bulletin of the Seismological Society of America*, vol. 101, pp. 1478–1487, Aug. 2011.
- [27] G. M. Harry, A. M. Gretarsson, P. R. Saulson, S. E. Kittelberger, S. D. Penn, W. J. Startin, S. Rowan, M. M. Fejer, D. R. M. Crooks, G. Cagnoli, J. Hough, and N. Nakagawa, “Thermal noise in interferometric gravitational wave detectors due to dielectric optical coatings,” *Classical and Quantum Gravity*, vol. 19, pp. 897–917, Mar. 2002.
- [28] A. E. Villar, E. D. Black, R. DeSalvo, K. G. Libbrecht, *et al.*, “Measurement of thermal noise in multilayer coatings with optimized layer thickness,” *Phys. Rev. D*, vol. 81, no. 16, p. 122001, 2010.
- [29] I. Martin, R. Bassiri, R. Nawrodt, M. M. Fejer, *et al.*, “Effect of heat treatment on mechanical dissipation in ta₂o₅ coatings,” *Class. Quantum Grav.*, vol. 27, p. 225020, 2010.
- [30] I. Martin, H. Armandula, C. Comtet, M. Fejer, *et al.*, “Measurements of a low-temperature mechanical dissipation peak in a single layer of ta₂o₅ doped with tio₂,” *Class. Quantum Grav.*, vol. 25, p. 055005, 2008.
- [31] F. Ya. and Khalili, “Reducing the mirrors coating noise in laser gravitational-wave antennae by means of double mirrors,” *Physics Letters A*, vol. 334, no. 1, pp. 67 – 72, 2005.
- [32] A. G. Gurkovsky, D. Heinert, S. Hild, R. Nawrodt, K. Somiya, S. P. Vyatchanin, and H. Wittel, “Reducing thermal noise in future gravitational wave detectors by employing khalili etalons,” *Physics Letters A*, vol. 375, no. 46, pp. 4147 – 4157, 2011.
- [33] G. M. Harry, M. R. Abernathy, A. E. Becerra-Toledo, H. Armandula, E. Black, K. Dooley, M. Eichenfield, C. Nwabugwu, A. Villar, D. R. M. Crooks, G. Cagnoli, J. Hough, C. R. How, I. MacLaren, P. Murray, S. Reid, S. Rowan, P. H. Sneddon, M. M. Fejer, R. Route, S. D. Penn, P. Ganau, J.-M. Mackowski, C. Michel, L. Pinard, and A. Remillieux, “Titania-doped tantala/silica coatings for gravitational-wave detection,” *Classical and Quantum Gravity*, vol. 24, pp. 405–415, Jan. 2007.
- [34] S. Penn, “Recent measurements of mechanical loss for aligo coating research.” LIGO document LIGO-G1000356, 2010.
- [35] X. Liu and R. O. Pohl, “Low-energy excitations in amorphous films of silicon and germanium,” *Phys. Rev. B*, vol. 58, pp. 9067–9081, 1998.
- [36] G. D. Cole, S. Groblacher, K. Gugler, S. Gigan, and M. Aspelmeyer, “Monocrystalline al_{[sub x]ga[sub 1 - x]} heterostructures for high-reflectivity high-q micromechanical resonators in the megahertz regime,” *Applied Physics Letters*, vol. 92, no. 26, p. 261108, 2008.
- [37] G. A. Golubenko, A. S. Svakhin, V. A. Sychugov, and A. V. Tishchenko, “Total reflection of light from a corrugated surface of a dielectric waveguide,” *Sov. J. Quantum Electron.*, vol. 15, no. 7, p. 886, 1985.
- [38] R. Magnusson and S. S. Wang, “New principle for optical filters,” *Appl. Phys. Lett.*, vol. 61, no. 9, pp. 1022–1024, 1992.
- [39] A. Bunkowski, O. Burmeister, D. Friedrich, K. Danzmann, and R. Schnabel, “High reflectivity grating waveguide coatings for 1064 nm,” *Classical and Quantum Gravity*, vol. 23, pp. 7297–7303, Dec. 2006.
- [40] D. Friedrich, B. W. Barr, F. Brückner, S. Hild, J. Nelson, J. Macarthur, M. V. Plissi, M. P. Edgar, S. H. Huttner, B. Sorazu, S. Kroker, M. Britzger, E.-B. Kley, K. Danzmann, A. Tünnermann, K. A. Strain, and R. Schnabel, “Waveguide grating mirror in a fully suspended 10 meter fabry-perot cavity,” *Opt. Express*, vol. 19, pp. 14955–14963, Aug 2011.



-
- [41] F. Brückner, D. Friedrich, T. Clausnitzer, O. Burmeister, M. Britzger, E.-B. Kley, K. Danzmann, A. Tünnermann, and R. Schnabel, “Demonstration of a cavity coupler based on a resonant waveguide grating,” *Opt. Express*, vol. 17, no. 1, pp. 163–169, 2009.
- [42] D. Friedrich, “Laser interferometry with coating-free mirrors,” 2011.
- [43] S. M. Norton, T. Erdogan, and M. G. Morris, “Coupled-mode theory of resonant-grating filters,” *J. Opt. Soc. Am. A*, vol. 14, pp. 629–639, 1997.
- [44] J.-Y. Vinet, “On special optical modes and thermal issues in advanced gravitational wave interferometric detectors,” *Living Reviews in Relativity*, vol. 12, no. 5, 2009.
- [45] J. Miller, *On Non-Gaussian Beams and Optomechanical Parametric Instabilities in Interferometric Gravitational Wave Detectors*. PhD thesis, University of Glasgow, 2010.
- [46] C. Bond, P. Fulda, L. Carbone, K. Kokeyama, and A. Freise, “Higher order Laguerre-Gauss mode degeneracy in realistic, high finesse cavities,” *Phys. Rev. D*, vol. 84, p. 102002, Nov. 2011.
- [47] T. Hong, J. Miller, H. Yamamoto, Y. Chen, and R. Adhikari, “Effects of mirror aberrations on laguerre-gaussian beams in interferometric gravitational-wave detectors,” *Phys. Rev. D*, vol. 84, p. 102001, Nov 2011.
- [48] B. J. Meers, “Recycling in laser-interferometric gravitational-wave detectors,” *Phys. Rev. D*, vol. 38, pp. 2317–2326, Oct. 1988.
- [49] S. Hild, H. Grote, M. Hewitson, H. Lück, J. R. Smith, K. A. Strain, B. Willke, and K. Danzmann, “Demonstration and comparison of tuned and detuned signal recycling in a large-scale gravitational wave detector,” *Classical and Quantum Gravity*, vol. 24, no. 6, pp. 1513–1523, 2007.
- [50] C. Caves, “Quantum-mechanical noise in an interferometer,” *Physical Review D*, vol. 23, pp. 1693–1708, 1981.
- [51] H. J. Kimble, Y. Levin, A. B. Matsko, K. S. Thorne, and S. P. Vyatchanin, “Conversion of conventional gravitational-wave interferometers into quantum nondemolition interferometers by modifying their input and/or output optics,” *Physical Review D*, vol. 65, pp. 022002–+, Jan. 2002.
- [52] V. B. Braginsky and F. Y. Khalili, “Quantum nondemolition measurements: the route from toys to tools,” *Rev. Mod. Phys.*, vol. 68, pp. 1–11, Jan 1996.
- [53] F. Y. Khalili, “The optical lever intracavity readout scheme for gravitational-wave antennae,” *Physics Letters A*, vol. 298, no. 5-6, pp. 308 – 314, 2002.
- [54] H. Rehbein, H. Müller-Ebhardt, K. Somiya, C. Li, R. Schnabel, K. Danzmann, and Y. Chen, “Local readout enhancement for detuned signal-recycling interferometers,” *Phys. Rev. D*, vol. 76, p. 062002, Sep 2007.
- [55] Y. Chen, “Sagnac interferometer as a speed-meter-type, quantum-nondemolition gravitational-wave detector,” *Phys. Rev. D*, vol. 67, pp. 122004–+, June 2003.
- [56] M. Stefszky and et al, “Balanced Homodyne Detection of Optical Quantum States at Audio-Band Frequencies and Below,” *in preparation*, 2011.
- [57] K. D. Skeldon, D. A. Clubley, G. P. Newton, S. Thieux, M. V. Gradowski, and B. W. Barr, “Measurements of an ultra-low loss polarizer for $\lambda = 1064$ nm using a high finesse optical cavity,” *Journal of Modern Optics*, vol. 48, no. 4, pp. 695–702, 2001.
- [58] F. Y. Khalili, “Quantum variational measurement in the next generation gravitational-wave detectors,” *Phys. Rev. D*, vol. 76, p. 102002, 2007.
- [59] H. J. Kimble, Y. Levin, A. B. Matsko, K. S. Thorne, and S. P. Vyatchanin, “Conversion of conventional gravitational-wave interferometers into quantum nondemolition interferometers by modifying their input and/or output optics,” *Phys. Rev. D*, vol. 65, p. 022002, 2001.



-
- [60] Harms, J. et al., “Squeezed-input, optical-spring, signal-recycled gravitational-wave detectors,” *Phys. Rev. D*, vol. 68, p. 042001, 2003.
- [61] D. Z. Anderson, J. C. Frisch, and C. S. Masser, “Mirror reflectometer based on optical cavity decay time,” *Appl. Opt.*, vol. 23, p. 1238, 1984.
- [62] G. Rempe, R. J. Thompson, H. J. Kimble, and R. Lalezari, “Measurement of ultralow losses in an optical interferometer,” *Opt. Lett.*, vol. 17, p. 363, 1992.
- [63] A. Ueda et al., “Ultra-High Quality Cavity with 1.5ppm Loss at 1064nm,” *Opt. Rev.*, vol. 3, p. 369, 1996.
- [64] A. Ueda, H. Yoneda, K. Ueda, K. Waseda, and M. O-Hashi, “Two-Dimensional Measurement of Optical Parameters of Superhigh-Quality Mirrors,” *Laser Physics*, vol. 8, p. 697, 1998.
- [65] Y. Chen, “Sagnac interferometer as a speed-meter-type, quantum-nondemolition gravitational-wave detector,” *Phys. Rev. D*, vol. 67, p. 122004, 2003.
- [66] H. Rehbein, H. Müller-Ebhardt, K. Somiya, S. L. Danilishin, R. Schnabel, K. Danzmann, and Y. Chen, “Double optical spring enhancement for gravitational-wave detectors,” *Phys. Rev. D*, vol. 78, p. 062003, Sep 2008.
- [67] Y. Chen, “Sagnac interferometer as a speed-meter-type, quantum-nondemolition gravitational-wave detector,” *Phys. Rev. D*, vol. 67, p. 122004, 2003.
- [68] H. Müller-Ebhardt, “On quantum effects in the dynamics of macroscopic test masses,” 2009.
- [69] C. Caves and B. Schumaker, “New formalism for two-photon quantum optics. i. quadrature phases and squeezed states,” *Phys. Rev. A*, vol. 31, pp. 3068–3092, 1985.
- [70] C. Caves and B. Schumaker, “New formalism for two-photon quantum optics. ii. mathematical foundation and compact notation,” *Phys. Rev. A*, vol. 31, pp. 3093–3111, 1985.
- [71] H. Kimble, Y. Levin, A. Matsko, K. Thorne, and S. Vyatchanin, “Conversion of conventional gravitational-wave interferometers into qnd interferometers by modifying their input and/or output optics,” *Phys. Rev. D*, vol. 65, 2002.
- [72] Y. Chen, S. Danilishin, F. Khalili, and H. Müller-Ebhardt, “Qnd measurements for future gravitational-wave detectors,” *General Relativity and Gravitation*, vol. 43, pp. 671–694, 2011.
- [73] J. Harms, Y. Chen, S. Chelkowski, A. Franzen, H. Vahlbruch, K. Danzmann, and R. Schnabel, “Squeezed-input, optical-spring, signal-recycled gravitational-wave detectors,” *Phys. Rev. D*, vol. 68, p. 042001, 2003.
- [74] P. Purdue and Y. Chen, “Practical speed meter designs for quantum nondemolition gravitational-wave interferometers,” *Phys. Rev. D*, vol. 66, p. 122004, 2002.
- [75] S. L. Danilishin, “Sensitivity limitations in optical speed meter topology of gravitational-wave antennas,” *Phys. Rev. D*, vol. 69, p. 102003, 2004.